UNIVERSITY OF OKLAHOMA

GRADUATE COLLEGE

INTERPRETATION OF GALVANIC RESISTIVITY, ELECTROMAGNETIC INDUCTION, AND DIELECTRIC DISPERSION LOGS TO ESTIMATE WATER SATURATION IN ORGANIC RICH SHALE

A THESIS

SUBMITTED TO THE GRADUATE FACULTY

in partial fulfillment of the requirements for the

Degree of

MASTER OF SCIENCE

By

PRATIKSHA TATHED
Norman, Oklahoma
2018

Downloaded from SHAREOK. Persistent Handle URL: https://hdl.handle.net/11244/316758

INTERPRETATION OF GALVANIC RESISTIVITY, ELECTROMAGNETIC INDUCTION, AND DIELECTRIC DISPERSION LOGS TO ESTIMATE WATER SATURATION IN ORGANIC RICH SHALE

A THESIS APPROVED FOR THE
MEWBOURNE SCHOOL OF PETROLEUM AND GEOLOGICAL ENGINEERING

BY

Dr. Siddharth Misra, Chair

Dr. Chandra S. Rai

Dr. Carl Sondergeld

© Copyright by PRATIKSHA TATHED 2018
All Rights Reserved.

Dedicated to my dear mom and dad who gave me countless love and support

Acknowledgements

My deepest gratitude goes first to my advisor, Dr. Siddharth Misra. Without his selfless help and guides, this research would not have been possible. I will be forever grateful for his constant encouragement, that has pushed me not only to dig deeper into my research, but also succeed in my career. I am forever indebted to my colleague, Yifu Han, for lending his time and support in developing this inversion work. He helped me a great deal in understanding the fundamentals of inversion work.

I would like to thank Dr. Chandra S. Rai and Dr. Carl Sondergeld, the members of my thesis committee, for shaping the course of my graduate program. I greatly appreciate their time in reviewing this work and making valuable suggestions and comments. I would also like to extend sincere thanks to IC^3 (Integrated Core Characterization Center) and my colleagues in IC^3 who have helped me immensely to conduct experiments.

I would like to thank my family, my parents, Ramesh Tathed, and Mangala Tathed who allowed me to move so far away to do all of this. My sisters and cousins who always encouraged me to focus on my research. Their unfailing support is exactly what I needed to accomplish my Master of Science degree at University of Oklahoma. I am indebted to my friends Pritesh Bhoumick, Yao Wang, and Gowtham Talluru for always supporting me, offering a helping hand and thoughtful advice. I would like to say thank you to Hao Li, He Jiabo, Sangcheol Yoon, and Shiv Prakash Ojha for their help in my research.

Table of Contents

Acknowledgements v

Table of Contents vi

List of Tables ix

List of Figures x

Abstract xv

1. Introduction 1

    1.1 Motivation and problem statement 1

    1.2 Objective of this study 2

    1.3 Organization of thesis 3

2. Methodology for the Inversion Scheme 4

    2.1 Abstract 4

    2.2 History of Inversion Schemes for EM Logs 4

    2.3 Dielectric Dispersion, Galvanic and Induction Logs 6

    2.4 EM Multifrequency dielectric models-SMD and CRIM 7

    2.5 Resistivity model - Waxman Smits and Simandoux 9

    2.6 Joint Inversion Methodology 10

    2.7 Conclusions 14

3. Sensitivity Analysis of Inversion Scheme 16

    3.1 Abstract 16

    3.2 Comparison of sensitivity of the proposed joint inversion with dielectric dispersion logs 16

    3.3 Uncertainties in inversion-derived estimates 20

    3.4 Effect of pyrite in low porosity high salinity formations 25

    3.5 Threshold of brine conductivity in WS, SMD, and CRI model 27

3.6 Conclusions 28
4. Synthetic Case Study and Field Case Study 30
4.1 Abstract 30
4.2 Synthetic Case Histograms and Model Predictions 30
4.3 Field Case Study 1 33
4.3.1 Wells in study and Characteristics 33
4.3.2 Log interpretation of our estimates 37
4.3.3 Error Analysis 38
4.4 Field Case Study 2 40
4.4.1 Wells in study and Characteristics 40
4.4.2 Log interpretation of our estimates 44
4.4.3 Error Analysis 46
4.5 Limitations of our work 47
5. Conclusions 49
Appendix A: Dielectric EM Laboratory Measurements on Sandstone Samples 56
A.1 Abstract 56
A.2 History of EM measurements on Sandstone 56
A.3 Samples Description 57
A.4 Measurements on saturated samples 58
A.4.1 Porosity 58
A.4.2 Saturation and NMR 59
A.4.3 Dielectric Equipment Calibration 59
A.4.4 Dielectric Measurement 60
A.5 Results 61
A.6 Conclusion 63
Appendix B: Laboratory Resistivity Measurements on Wolfcamp Shale Samples 65

B.1 Abstract 65
B.2 History of resistivity measurements on shale 65
B.3 Samples Description 66
B.4 Measurements on saturated samples 68
B.4.1 Saturation and NMR 68
B.4.2 Resistivity Measurement 68
B.5 Experiment Results 69
B.5.1 Effect of confining pressure and equilibrium time 69
B.5.2 Resistivity and porosity 69
B.6 Conclusions 72

List of Tables

Table 4-1: Petrophysical parameters assumed for synthetic case study 31

Table A.1 Dimensions of 14 Berea Sandstone samples.....58

Table B.1 Dimensions of 5 Wolfcamp samples.....67

List of Figures

Figure 2.1 Log processing workflow 14

Figure 3.1 Comparison of sensitivity of (a & c) integrated CRIM and SMD model used for dielectric dispersion inversion against that of (b & d) integrated CRIM, SMD and WS model used for the newly proposed joint inversion to variations in in $S_w$and C_w around the default parameters: m=2, n=2, C_w=10 S/m, φ_t=0.02, BQ_v=1.3 mS/cc, and S_w=0.3 s.u. and around the default parameters: m=2, n=2, C_w=10 S/m, φ_t=0.02, BQ_v=1.3 mS/cc, and S_w=0.9 s.u., respectively.. 18

Figure 3.2 Comparison of sensitivity of (a & c) integrated CRIM and SMD model used for dielectric dispersion inversion against that of (b & d) integrated CRIM, SMD and WS model used for the newly proposed joint inversion to variations in n and m around the default parameters: m=2, n=2, C_w=10 S/m, φ_t=0.05, BQ_v=1.3 mS/cc, and S_w=0.3 s.u. and around the default parameters: m=2, n=2, C_w=10 S/m, φ_t=0.05, BQ_v=1.3 mS/cc, and S_w=0.9 s.u., respectively 20

Figure 3.3 Comparison of sensitivities of the integrated CRIM, SMD and WS model to variations in n and C_w for (a) S_w=0.2, (b) S_w=0.5, (c) S_w=0.9, and (d) S_w=0.99 around default parameters: n =2,m=2, φ_t=0.05, C_w=10 S/m, and BQ_v=1.3 mS/cc..... 22

Figure 3.4 Comparison of sensitivities of the integrated CRIM, SMD and WS model to variations in m and S_w for (a) n=2,C_w=10 S/m; (b) n=3,C_w=10 S/m; (c) n=4,C_w=10 S/m; and (d) n=2,C_w=20 S/m around the default parameters: m=2, φ_t=0.05, S_w=0.9 s.u. and BQ_v=1.3 mS/cc. . 23

Figure 3.5 Comparison of sensitivity of (a) integrated CRIM and SMD model for dielectric dispersion inversion against that of (b) integrated CRIM, SMD and WS model for the proposed

joint inversion to variations in φ_t and $C_w$around default parameters: $n = 2, m = 2, \varphi_t = 0.02, C_w = 10\ S/m$ and $Sw = 0.3$ 24

Figure 3.6 Comparison of sensitivity of (a) integrated CRIM and SMD model for dielectric dispersion inversion against that of (b) integrated CRIM, SMD and WS model for the proposed joint inversion to variations in φ_t and C_w around default parameters: $n = 2, m = 2, \varphi_t = 0.02, C_w = 10\ S/m$ and $Sw = 0.6$ 25

Figure 3.7 Comparison of sensitivity of (a) the integrated CRIM and SMD model used for dielectric dispersion inversion against that of (b) the integrated CRIM, SMD and WS model used for the proposed joint inversion to variations S_w and V_{py} around the default parameters: n=2, m=2, φ_t=0.02,C_w=10 S/m, V_{py}=0.02, BQ_v=1.3 mS/cc, and S_w=0.3 s.u 26

Figure 3.8 Comparison of sensitivity of (a) the integrated CRIM and SMD model used for dielectric dispersion inversion against that of (b) the integrated CRIM, SMD and WS model used for the proposed joint inversion to variations S_w and V_{py} around the default parameters: n=2, m=2, φ_t=0.02,C_w=10 S/m, V_{py}=0.02, BQ_v=1.3 mS/cc, and S_w=0.3 s.u 27

Figure 3.9 Comparison of sensitivity of resistivity at 20 kHz and permittivity and conductivity dispersions at frequencies: F0 (22 MHz), F1 (100 MHz), F2 (350 MHz) and F3 (1 GHz) to brine conductivity for (a) water rich layer of S_w=0.9 s.u. (b) oil-rich layer of S_w=0.1 s.u. and (c) clay-rich layer of S_w=0.9 s.u. and Vc=40% with default parameters m=2, n=2, φ_t=0.07, and BQ_v=75 mS/cc..... 28

Figure 4.1 Frequency of occurrence of the inversion-derived estimates of (a) C_w, (b) S_w, (c) $m = 2$, and (d) $n = 2$ with relative errors in matching the synthetic data for 250 random initializations of the proposed joint inversion of synthetic data, shown in Figure 4.2. 32

Figure 4.2 Comparison of synthetic effective conductivity, relative permittivity, and resistivity data and the integrated model predictions based on the inversion-derived estimates. .. 33

Figure 4.3 Track 1 is the depth (XX060-XX130) and formation type, Track 2 is the gamma ray (GR) and caliper (CAL), Track 3 is the laterolog resistivity (RLA), Track 4 contains the neutron porosity (NEU), bulk density (DEN), and total porosity (PHIT), Track 5 contains volume fractions of various minerals: quartz, chlorite, kerogen, pyrite, and calcite, Track 6 contains inversion-derived brine conductivity (C_w) estimate with a range, Track 7 contains water saturation estimated using various methods (S_w), Track 8 contains inversion-derived cementation exponent estimate (m) estimate with a range, Track 9 contains inversion-derived saturation exponent estimate (n) estimate with a range, Track 10 contains relative errors in dielectric and induction model, Track 11 contains measured (bold) and modeled (dash) permittivity dispersion logs at four frequencies, and Track 12 contains measured (bold) and modeled (dash) conductivity logs at four frequencies. 35

Figure 4.4 Logs for formation depth from XX322 to XX360. The logs and the layout presented in this figure are similar to those in Figure 4.3. Track 13 contains T2 NMR distribution 36

Figure 4.5. Logs for formation depth from XX412 to XX450. The logs and the layout presented in this figure are similar to those in Figure 4.3. 36

Figure 4.7 Track 1 is the formation type, Track 2 is the depth (XX610-XX670 ft), Track 3 is the gamma ray (GR), Track 4 contains the induction resistivity (AT), horizontal resistivity R_h, vertical resistivity R_v and modeled resistivity , Track 5 contains the bulk density (RHOZ), neutron porosity (TNPH), and total porosity (PHIT), Track 6 contains volume fractions of various minerals: quartz, dolomite, calcite, pyrite, chlorite, illite and montmorillonite, Track 7 contains anisotropy logs derived from Rt scanner, Track 8 contains inversion-derived brine conductivity (C_w) estimate with

a range, Track 9 contains water saturation estimated using various methods (S_w), Track 10 contains inversion-derived cementation exponent estimate (m) estimate with a range, Track 11 contains inversion-derived saturation exponent estimate (n) estimate with a range, Track 12 contains relative errors in dielectric and induction model, Track 13 contains measured (bold) and modeled (dash) permittivity dispersion logs at four frequencies, Track 14 contains measured (bold) and modeled (dash) conductivity logs at four frequencies, and Track 15 contains NMR T2 distribution. 42

Figure 4.8 Logs for formation interval from the depth of XX710 to XX766 ft. The logs and the layout presented in this figure are similar to those in Figure 6.6. 43

Figure 4.9 Logs for formation interval from the depth of XX780 to XX850 ft. The logs and the layout presented in this figure are similar to those in Figure 6.6. 43

Figure A.1 Dielectric Fixture 16451B and Impedance Analyzer E4990A setup 60

Figure A.2 (a) Porosity at various confining pressures and (b) NMR measured values of incremental and cumulative porosities for sample S1 62

Figure A.3 (a) Magnitude and (b) phase of relative permittivity of dry, DI-water-saturated and brine-water saturated samples: S1(circle), S2diamond), S3(plus), S4(asterisk), S5(triangle), S6(cross), and S7(square). 63

Figure B.1 FTIR Mineralogy of Wolfcamp samples 67

Figure B.2 (a) Real part of resistivity (b) Imaginary part of resistivity for samples 242H, 245H, 252H, 256H and 259H 70

Figure B.3 Relative resistivity changes with frequency for (a) sample 242H at 3500psi confining pressure and (b) sample 252H at 4500psi confining pressure and 2 hours of equilibrium time. 70

Figure B.4 Cross-plot of (a) resistivity and porosity for Wolfcamp samples at 1000Hz frequency (b) formation factor and porosity on log-log scale at 1000Hz frequency..... 71

Figure B.5 Cross-plot of (a) cementation exponent and porosity for Wolfcamp samples (b) cementation exponent and total organic carbon..... 72

Abstract

Water saturation estimation based on electrical and electromagnetic logs in organic-rich shale reservoirs is challenging due to effects of clay and conductive minerals. Presence of nanopores, low porosity, interfacial polarization effects, and highly anisotropic tortuous paths in organic-rich shales and tight hydrocarbon-bearing formations results in breakdown of conventional models for purposes of water saturation estimation. These petrophysical attributes lead to disagreement between water saturation estimates obtained using different approaches, such as Nuclear Magnetic Resonance (NMR), Induction, Dielectric, and Dean-Stark retort measurement method. Few of the above-mentioned challenges in water saturation estimation can be addressed by jointly processing the subsurface galvanic resistivity, induction, propagation and dielectric dispersion logs using an integrated mechanistic model that accounts for various frequency-dependent interfacial polarization mechanisms.

Single-frequency galvanic resistivity (laterolog) or single-frequency induction resistivity and multi-frequency dielectric dispersion logs, comprising 4 conductivity and 4 dielectric permittivity logs measured at four distinct frequencies were acquired in few wellbores drilled in Wolfcamp and Bakken shale formations. We implement a novel log-interpretation technique for the improved estimation of water saturation (S_w), brine conductivity (C_w), textural index/cementation exponent (m), and saturation exponent (n). The proposed log-processing workflow uses an integrated mechanistic model, which combines Complex Refractive Index (CRI) model to analyze the conductivity and permittivity logs acquired at 1 GHz, Stroud-Milton-De (SMD) model to analyze the 3 conductivity dispersion and 3 permittivity dispersion logs in the frequency range of 10 MHz to 0.3 GHz, and Waxman-Smits (WS) model to analyze the single-frequency deep galvanic resistivity log (RLA5) acquired at 1 kHz or the single-frequency induction resistivity (AT90) log

acquired at 20 kHz. Petrophysical estimates derived from the joint inversion were robust in the presence of pyrite, low water saturation, and low porosity as compared to the petrophysical estimates from the inversion of only four-frequency dielectric dispersion logs or those from the single-frequency resistivity log.

Based on the petrophysical estimates from the proposed methodology, formation brine conductivity and saturation-exponent estimates are more reliable compared to water saturation and cementation exponent estimates. Water saturation estimates obtained using the proposed methodology are compared against those obtained using multi-mineral inversion and CRIM model and those from NMR log, Dean-Stark core measurements and service company's dielectric inversion. Average relative errors in fitting the 1 laterolog resistivity and 8 dielectric dispersion logs using the estimates obtained from the proposed method are 10% and 20%, respectively, and their extreme values are 55% and 60%, respectively, in the 520-ft depth interval of the upper Wolfcamp shale formation. Average relative errors in matching the 1 induction resistivity and 8 dielectric dispersion logs using the inversion-derived estimates are 33% and 20%, respectively, in the 350-ft depth interval of Bakken Petroleum System (BPS).

Water saturation and formation brine conductivity estimates in Middle Bakken are in the ranges of 0.5 to 1 and 25 S/m to 45 S/m, respectively. In the Upper Wolfcamp formation, water saturation estimates are in the range of 0.4 to 1 and connate water conductivity are in the range of 5 S/m to 30 S/m.

1. Introduction

This thesis presents work performed for a Master of Science degree that was conducted at Mewbourne School of Petroleum and Geological Engineering of the University of Oklahoma. The research presented herein firstly emphasizes on the dielectric laboratory measurements on sandstone samples and resistivity measurements on shale samples. It further introduces sensitivity analysis for inversion schemes combining resistivity and dielectric models. The inversion scheme has been applied in unconventional reservoirs of Upper Wolfcamp in Delaware Basin and Bakken Petroleum System to estimate petrophysical properties of these formations. The following sections present the motivation and problem statement, objective, and organization of this thesis.

1.1 Motivation and problem statement

Water saturation (S_w) and hydrocarbon saturation ($S_{hc} = 1 - S_w$) estimates in hydrocarbon-bearing formations are generally derived from Dean-Stark core measurements, Nuclear Magnetic Resonance (NMR) log, and electromagnetic (EM) logs, such as induction log, galvanic resistivity (laterolog), or dielectric dispersion logs. In-situ estimation of hydrocarbon saturation in conventional reservoirs primarily rely on the deep-sensing or high-resolution EM logs. However, in the hydrocarbon-bearing shale formations, hydrocarbon saturation estimates obtained from EM logs tend to be unreliable. Conventional EM-log-interpretation models tend to break down for shale formations because they neglect the interfacial polarization effects and the dispersive behaviour of EM properties of such geomaterials. Processing techniques used to derive estimates from service company inversion techniques have limited information available. Service company's dielectric inversion results provide water saturation estimates with an exact value instead of range of possible values within a desired accuracy. In unconventional reservoirs of Delaware basin, water saturation estimation is difficult due to complex mineralogy, higher clay

content, low porosity, textural features and high salinity. Similarly, Bakken Petroleum System (BPS) is composed of both conventional and unconventional units, which exhibits significant variations in lithology, rock texture, dolomite content, clay content, total organic carbon, accompanied by high connate water salinity, presence of disseminated pyrite grains, and low values of porosity. These petrophysical attributes of the BPS lead to inconsistency in the oil-in-place estimates for those obtained from Electromagnetic (EM) induction log, (NMR) log, dielectric dispersion log measured by Array Dielectric Tool (ADT), and Dean-Stark core measurements.

Interpretation with only 1-GHz dielectric permittivity log or with only laterolog or induction resistivity log or with only 8 dielectric dispersion logs in the frequency range of 10 MHz to 1 GHz is sensitive to model assumptions, noise in data, noise in model inputs, interfacial polarization mechanisms, textural effects, and has low sensitivity to certain petrophysical properties. These challenges can be addressed by performing a joint processing of resistivity and dielectric dispersion logs using an integrated mechanistic model.

1.2 Objective of this study

(1) Perform electrical resistivity measurements on shale core samples at low frequencies to estimate formation petrophysical properties

(2) Develop a joint petrophysical interpretation of multifrequency resistivity and dielectric permittivity logs acquired in clay- and pyrite-rich shale formations

(3) Understand sensitivity and robustness of our proposed log-processing technique that jointly inverts the multifrequency resistivity and dielectric permittivity logs

1.3 Organization of thesis

The following is an outline and brief description of the remainder this thesis:

Chapter 2 introduces dielectric and resistivity models implemented in the newly proposed log-inversion technique and the inversion methodology used to estimate the petrophysical properties;

Chapter 3 discusses the sensitivity of the proposed inversion technique for joint processing of the multifrequency resistivity and dielectric permittivity logs;

Chapter 4 presents the application of the newly proposed inversion-based petrophysical interpretation to Upper Wolfcamp shale formation and Bakken Petroleum System;

Chapter 5 includes conclusions that can be drawn from the results presented in previous chapters and recommendations for future work;

Appendix A contains literature review about the EM measurements on sandstone samples and laboratory dielectric measurements on Berea sandstone;

Appendix B introduces laboratory resistivity measurements on Wolfcamp shale samples and their petrophysical interpretation.

2. Methodology for the Joint Inversion of Galvanic Resistivity, Electromagnetic Induction Resistivity, and Dielectric Dispersion Logs

2.1 Abstract

This chapter introduces various inversion schemes for Electromagnetic (EM) logs, and the physics controlling the dielectric, galvanic (laterolog) and the EM induction measurements. We further describe dielectric and resistivity models implemented in the newly proposed log-inversion technique and the inversion methodology used to estimate the petrophysical properties.

2.2 History of Inversion Schemes for EM Logs

Sarihi and Murillo (2015) proposed a workflow to estimate water saturation using Waxman-Smits (WS) equation in tight-gas formations considering the conductivity and volume fraction of clay minerals. Their results on tight rock samples indicated a proportional relationship between clay content and the clay factor, which replaced BQ_v in the WS equation and was recommended for shale evaluation. Donadille et al. (2016) addressed the limitations in determining high connate-water salinity with dielectric logs. At high salinity of about 70,000 ppm, the dielectric measurements lose sensitivity to salinity. Joint inversion of neutron sigma measurements and dielectric dispersion logs showed excellent sensitivity to high salinity values in Bakken shale formation. Chen and Heidari (2014) proposed joint interpretation of dielectric and resistivity measurements that significantly improves water-filled porosity and hydrocarbon saturation assessment. They introduced analytical model combining conductivity and permittivity measurements for organic-rich source rocks with complex pore structure. They suggested that spatial distribution and tortuosity of water, kerogen, and pyrite networks significantly affect dielectric permittivity and electrical resistivity.

Han and Misra (2018a) explain the complexity of analyzing dispersion measurements and introduce new inversion schemes and their sensitivity to various forms of noise. Han et al. (2017) and Han and Misra (2018b) proposed a log processing methodology by combining Lichtenecker–Rother model, Stroud-Milton De model, and PS model, a mechanistic pyrite-clay dispersion model, for the estimation of water saturation, formation water salinity, homogeneity index, and cementation index in clay-lean and clay-rich units of Bakken shale. They carried their interpretation for a 300-feet depth interval in Bakken Petroleum System (BPS) and compared their estimates with Dean Stark core water saturation, (Nuclear Magnetic Resonance) NMR

interpretation and service company's inversion results. Misra and Han (2016) carried out joint interpretation using conductivity and permittivity values obtained from EM induction at 26 kHz, EM propagation at 400kHz and 2MHz, and dielectric dispersion logs at 20 MHz, 100 MHz, 260 MHz, and 1 GHz to estimate the water saturation, bulk conductivity of brine, surface conductance of clay, and radius of spherical clay grains. This work was further improved by Han and Misra (2018c) to develop robust inversion methodology for jointly processing galvanic, induction, propagation, and dielectric dispersion logs.

Pirie et al. (2016) compared water saturation estimates obtained from triaxial resistivity induction log, NMR log, dielectric dispersion log, Techlog Quanti-ELAN, and Dean-Stark core measurements. S_w evaluated with the petrophysical model using R_h from induction resistivity logs at 2-ft vertical resolution is 5% saturation unit offset with S_w obtained from dielectric measurements in Middle Bakken. The Dean-Stark core water saturation ranged from 40-60 % in lower portion of Three Forks formation while dielectric measurements suggested 100 % water saturation.

2.3 Dielectric Dispersion, Galvanic, and Induction Logs

The induction log uses a high frequency current flowing in a coil to induce a current in the formation that flows circumferentially around the tool axis (Misra et al., 2016c). Induction measurements are related to the electrical conductivity of the formation. Induction tools are generally recommended for wells drilled with oil-based muds. The AIT array induction tool generates resistivity logs from measurements at five different depths of investigation (DOIs)—10, 20, 30, 60, and 90 inches with vertical resolution ranging from 1 to 4 ft. The differences between these curves enable accurate assessment of true formation resistivity, R_t, free from the effects of shallow invaded zone.

Laterolog resistivity tool injects electric currents into geological formations and records the potential drop across a specific length along the openhole well. Laterolog measurements are related to the electrical resistivity of the formation. Laterolog tools are reliable in boreholes drilled with water-based muds. Laterolog tool has 2-feet resolution with 10, 20, 30, 60 and 90 inches of depths of investigation and operates at frequencies less than 10kHz. On the other hand, dielectric dispersion tool transmits EM waves and records the changes in amplitudes and the phases of the propagating wave, which are related to the dielectric permittivity and electrical conductivity of the formation and their dispersive behaviors (Han et al., 2017). Dielectric dispersion tool has 1-inch vertical resolution and operates at multiple discrete frequencies in the range of 10MHz to 1GHz.

2.4 EM Multifrequency dielectric models-SMD and CRIM

Interpretation of laterolog tool focuses on the petrophysical controls on charge transport through porous media, which can be formulated like Archie's or Waxman-Smits (WS) type equations. Interpretation of dielectric tool is based on the large contrast between permittivity of water and that of oil and rock minerals (Chan and Knight, 1999). This interpretation primarily focusses on the petrophysical controls on charge storage, accumulation, and relaxation; thereby, facilitating water volume estimation independent of water salinity. In this study, the joint inversion technique processes low-frequency laterolog measurements using WS model, the two 1-GHz conductivity and permittivity logs using CRI (Complex-refractive index) model, and the three-conductivity dispersion and three permittivity dispersion logs acquired in the range of 20 MHz to 0.3 GHz using SMD (Stroud-Milton-De) model. CRI model is a commonly used single-frequency model for subsurface dielectric characterization at high frequencies close to 1 GHz. It is derived from the Lichteneker-Rother (LR) model which can be expressed as (Sabouroux and Ba, 2011),

$$(\varepsilon_b^*)^\alpha = (1- \varphi_t)(\varepsilon_m)^\alpha + S_w \varphi_t (\varepsilon_w^*)^\alpha + (1 - S_w)\varphi_t (\varepsilon_o)^\alpha \quad (2.1)$$

where ε_b^* is the bulk complex permittivity of the formation, ε_m is the matrix permittivity, ε_w^* is the complex permittivity of water, ε_o is the hydrocarbon permittivity, φ_t is the total porosity, S_w is water saturation, and α is the geometrical fitting parameter ranging from -1 to 1. With α = 0.5, the Equation 2.1 becomes the CRI model. In our work, one simplifying assumption is α = 0.5 indicating a homogenous mixture without layering. CRI model does not consider the structure and spatial distribution of rock components (Brovelli and Cassiani, 2008)

Stroud et al. (1986) introduced an analytical mixing formula to calculate complex dielectric permittivity and its dispersion in brine-saturated rocks as a function of total porosity, water saturation, dielectric permittivities of rock matrix, brine, and oil, rock textural parameter (m') that describes cementation/tortuosity, and brine conductivity. SMD model is expressed as

$$\varepsilon_b^* = (\varphi_t S_w)^{m'} \varepsilon_w^*(C_w) + \left[1 - (\varphi_t S_w)^{m'}\right]\varepsilon_{mo} \; - \; \varepsilon_{mo}\, \Gamma\left(\varphi_t S_w, m', \frac{\varepsilon_w^*(C_w)}{\varepsilon_{mo}}\right) \quad (2.2)$$

where

$$(\varepsilon_m)^\alpha = \frac{(1 - \varphi_t)(\varepsilon_m)^\alpha + (1 - S_w)\varphi_t(\varepsilon_o)^\alpha}{1 - \varphi_t S_w} \quad (2.3)$$

$$\varepsilon_w^*(C_w) = \varepsilon_b + i\frac{C_w}{\varepsilon_0 \omega} \quad (2.4)$$

where

ε indicates relative permittivity, $\varepsilon_b = 80$, $\varepsilon_0 = 8.85 \times 10^{-12}$ F/m, and $\omega = 2\pi f$ with f = 20, 100 and 300 MHz.

Water permittivity decreases with increasing temperature as thermal agitation reduces the overall alignment of the molecules along the field direction. Water permittivity can be expressed as (Stroud et al., 1986)

$$\varepsilon_w^*(S,T) = \left[\frac{1}{\varepsilon_w^*(0,T)} + \frac{2.4372 * S}{58.443(1000 - S)}\right]^{-1} \quad (2.5)$$

where S is the salinity expressed in kppm, and $\varepsilon_w^*(0,T)$ is water permittivity corrected for the effect of temperature expressed as,

$$\varepsilon_w^*(0,T) = 94.88 - 0.2317T + 0.000217T^2 \quad (2.6)$$

Where T is temperature in °F, T = 232°F for this well.

The empirical equation of water conductivity C_w with temperature and salinity used in this paper can be expressed as (Stroud et al., 1986),

$$C_w(S,T) = \frac{T+7}{82}\left(0.0123 + \frac{3647.5}{(1000 * S)^{0.955}}\right)^{-1} \quad (2.7)$$

We assume $\boldsymbol{m'} = \boldsymbol{m}$, i.e. textural index is equivalent to cementation exponent, in SMD model for purposes of simplifying the joint log processing. In strict terms, SMD model was not developed for clay- and pyrite-rich formations. Also, the integrated LR, CRIM, and SMD model neglects the interfacial polarization (IP) effects of clays and conductive minerals in the shale formation.

2.5 Resistivity model - Waxman Smits

Waxman and Smits (1968) introduced a resistivity-based model for clay-rich geomaterials to estimate water saturation by accounting for additional conductivity due to the presence of clay with high cation exchange capacity (CEC). WS model is expressed as,

$$\frac{1}{R_t} = \varphi_t^m S_w^n \left(C_w + \frac{B.Q_v}{S_w} \right) \quad (2.8)$$

where R_t represents the true resistivity of the formation, φ_t is the total porosity, S_w is water saturation, C_w is the brine conductivity in S/m, Q_v is the cation exchange capacity (CEC) per unit pore volume in meq/cc, B is the equivalent conductance of sodium clay exchange cations in mS/meq which depends on the salinity of brine and temperature of formation, m is the cementation exponent and n is the saturation exponent. Peeters and Holmes (2014) showed that WS method is not very sensitive to variation of most of the parameters when B is fixed and reliable $Q_v$values are used. Based on the temperature of the formation and an estimate of salinity of brine provided by the operator company, B value was fixed to 13 mS/meq. For further simplification, Q_v was assumed to be 0.1 meq/cc based on the typical value suggested by the operator company. In future work, we will allow variable Q_v and B based on depth-wise clay types and their volume fractions. WS model focuses on dispersed shaly-sand and does not account for the effects of shale laminations and thin beds.

2.6 Joint Inversion Methodology

Han and Misra (2018a) and Han and Misra (2018c) proposed a joint-interpretation method using Modified Levenberg-Marquardt algorithm (LMA) for deriving accurate water-saturation estimates in pyrite-and clay rich-formations. A similar inversion scheme is used by Han and Misra (2018b) to process dispersive electrical conductivity and dielectric permittivity logs and compute range of water saturation estimates in Bakken Petroleum System (BPS). In this work, similar LMA inversion scheme have been used combining mechanistic models, for the estimation of water saturation, formation water salinity, saturation exponent, and cementation index.

We developed a joint inversion technique to jointly process 9 EM logs, 1 laterolog resistivity/1 induction resistivity and 8 dielectric dispersion logs, to estimate S_w, C_w, m, and n, with associated ranges of possible values (Figure 2.1). The estimates are generated at a vertical resolution of 2 inch. The joint inversion scheme is coupled to WS, SMD, and CRI models.

Measured data vector v, comprising 1 $Res^{\text{meas,1kHz}}$, 4 $Perm^{\text{meas,f}_i}$, and 4 $Cond^{\text{meas,f}_i}$, is jointly inverted in the proposed log-processing scheme. $Res^{\text{meas,1kHz}}$ represents the true resistivity of the formation measured using the galvanic resistivity (laterolog) tool at 1 kHz. $Perm^{\text{meas,f}_i}$ and $Cond^{\text{meas,f}_i}$ represent effective permittivity and conductivity of formation measured at 4 distinct dielectric-dispersion log-acquisition frequencies of $f_2 < f_3 < f_4 < f_5$.The objective is to estimate petrophysical model parameter vector p comprising water saturation (S_w), formation water conductivity(C_w), homogeneity index (m), and saturation exponent (n). A joint inversion is implemented to process the measured data vector v to estimate the model parameter vector p. The inversion scheme is coupled with an integrated mechanistic model, which combines CRI, SMD and WS models, to estimate the petrophysical parameters in vector p. The joint inversion scheme is initiated using 250 random guesses for the parameters in vector p, namely $S_w, C_w, m,$ and n.

The measured data vector v comprising galvanic resistivity, dielectric permittivity dispersions, and electrical conductivity dispersions are matched with modeled data vector m computed using the integrated CRI, SMD, and WS model. Various values of the vector m can be generated by varying the model parameter vector p. To that end, the Levenberg Marquardt algorithm (LMA) inversion algorithm iteratively computes the vector p for finding the best match that directs the convergence towards the optimum estimates for the unknown model parameters in vector p. This best estimate of vector p generates best fit between the measured data vector v and modeled data vector m, thus

minimizing the data misfit. This inversion scheme requires minimization of cost function vector denoted as $F(p)$. Individual components of the vector $F(p^k)$ at the k-th iteration are denoted as $f_l(p^k)$, where the superscript k is the iteration counter for the inversion scheme, pk is the model parameter vector computed at the k-th iteration of the LMA-based inversion, and subscript *l* denotes one of the 9 EM log. $F(p^k)$is divided by the standard deviation of the nine EM logs for robust parameter estimation. Cost function vector at *k*-th iteration $F(p^k)$ is expressed as

$$F(p^k) = [f_1(p^k), f_2(p^k), \dots f_9(p^k)]^T \tag{2.9}$$

where $f_l(p^k)$ is expressed as

$$f_1(p^k) = [Res^{mod,1kHz}(p^k) - Res^{meas,1kHz}] \tag{2.10}$$

for l = 2, 3, 4, and 5

$$f_l(p^k) = [Perm^{mod,f_i}(p^k) - Perm^{meas,f_i}] \tag{2.11}$$

at 4 distinct dielectric-dispersion log-acquisition frequencies of $f_2 < f_3 < f_4 < f_5$.

and for l = 6, 7, 8, and 9

$$f_l(p^k) = [Cond^{mod,f_i}(p^k) - Cond^{meas,f_i}] \tag{2.12}$$

at 4 distinct dielectric-dispersion log-acquisition frequencies of $f_2 < f_3 < f_4 < f_5$.

The Jacobian matrix of $F(p^k)$ is formulated as

$$J(p^k) = \begin{pmatrix} \frac{\partial f_1(p^k)}{\partial p_1^k} & \dots & \frac{\partial f_1(p^k)}{\partial p_4^k} \\ \vdots & \ddots & \vdots \\ \frac{\partial f_9(p^k)}{\partial p_1^k} & \dots & \frac{\partial f_9(p^k)}{\partial p_4^k} \end{pmatrix} \tag{2.13}$$

where $p^k = [p_1^k; p_2^k; p_3^k; p_4^k]$.

We implemented the first order central-difference formula to approximate the derivative of $f_l(p^k)$ with respect to the *j*-th unknown parameters formulated as

$$\frac{\partial f_l(p^k)}{\partial p_j^k} \approx \frac{f_l\left(p_j^k + \Delta p_j^k\right) - f_l\left(p_j^k - \Delta p_j^k\right)}{2\Delta p_j^k} \tag{2.14}$$

such that Δp_j^k=0.001p_j^k, $1 \leq j \leq 4$ representing the index for model parameters, and $1 \leq l \leq 9$ representing the index for the 9 EM log.

After convergence, a line search method is applied to find the smallest error in the search space to select the estimates for the unknown model parameters, S_w, C_w, m, and n, in the vector p that generates the least data misfit. The search for global minimum among the 250 inversion searches is affected by the noise in the data and uncertainties in the inputs to the three models, namely CRI, SMD, and WS models, coupled with the inversion scheme. Therefore, we generate ranges of possible values for the unknown model parameters rather than a single estimate. To that end, all possible values of the unknown model parameters, namely S_w, C_w, m, and n, are searched around global minimum that lead to data misfit within the predefined fitting error that does not exceed 1.1 times the data misfit at the global minimum. This generates minimum and maximum values for the four inversion-derived estimates.

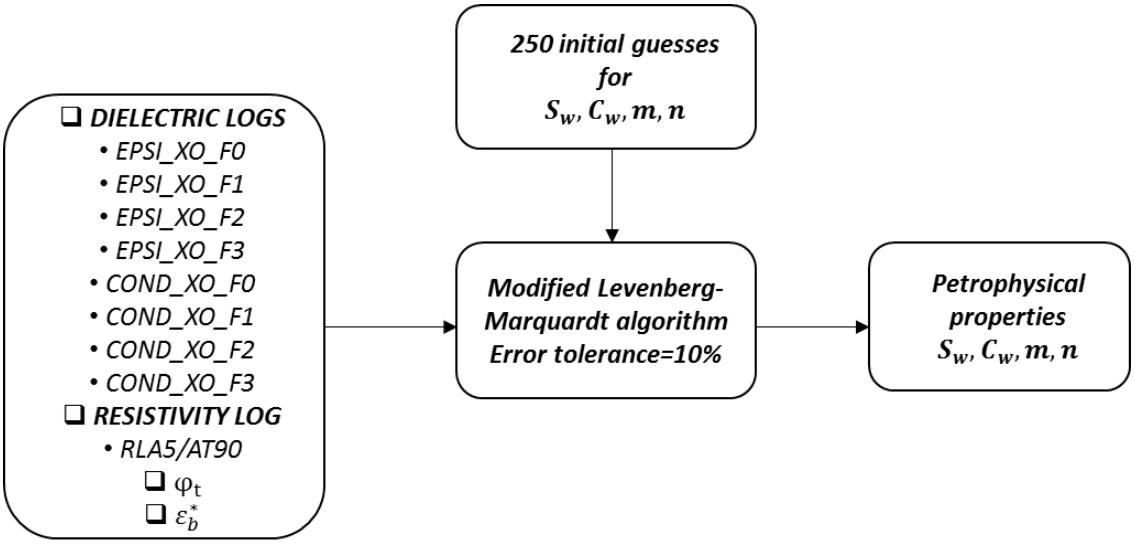

Figure 2.1 Log processing workflow

The total porosity used for water saturation estimation is computed using ELAN multi-mineral inversion of resistivity, gamma-ray, density, neutron, sonic, and elemental spectroscopy data (Ferraris et al., 2012). The computations for total porosity are based on a probabilistic approach combining the above-mentioned logs with constraints of TOC (Total Organic Carbon), calcite transform, and pyrite transform.

2.7 Conclusions

We introduced first-of-its-kind joint inversion of laterolog resistivity and dielectric dispersion logs at multiple frequencies. The joint inversion methodology combines 9 EM logs, 1 laterolog resistivity/1 induction resistivity, and 8 dielectric dispersion logs, to estimate S_w, C_w, m, and n, along with associated uncertainty. In doing so, effects of interfacial polarization due to clays, pyrite, and pore structure can be better characterized for accurate estimation of hydrocarbon saturation. Without dielectric dispersion logs, only laterolog resistivity could be used to estimate water saturation; nonetheless, there will be an unaccounted large interfacial polarization effect that will reduce the accuracy of the hydrocarbon saturation estimation. The dielectric models and the

resistivity models used in this inversion scheme and their associated limitations have been described for reference. All possible values of the unknown model parameters, namely S_w, C_w, m, and n, are searched around the global minimum such that data misfit does not exceed 1.1 times the data misfit at the global minimum.

3. Sensitivity of the Proposed Joint Inversion Scheme

3.1 Abstract

Uncertainty of the inversion-derived estimates could be indicated with the spread of minima around the global minimum. We understand the robustness and the sensitivity of the proposed inversion technique to jointly process the multifrequency resistivity and dielectric permittivity logs. We compare sensitivity of the proposed inversion technique to replicate reservoir formation with low porosity, high pyrite content and high clay content.

3.2 Comparison of sensitivity of the proposed joint inversion with dielectric dispersion logs

Uncertainty analysis evaluates uncertainty in model components. The objective of sensitivity analysis is to determine how sensitivity the output of the model is with respect to elements of the model that are subjected to uncertainty. We study the sensitivity analysis of the integrated model by changing combination of variables simultaneously to learn more about the robustness of the results to widespread changes around the global minimum. The following sensitivity analysis is closely related to error propagation. We couple the error minimization (inversion) workflow with the integrated Waxman-Smits (WS), Stroud-Milton-De (SMD), and Complex Refractive Index (CRI) model to process the 9 EM logs. Sensitivity of the integrated WS, SMD, and CRI model is compared against that of the integrated SMD and CRI model, required to process only the dielectric dispersion logs. We vary the brine conductivity in the range of 5 S/m to 25 S/m and water saturation in the range of 0.1 to 1 saturation unit (s.u.) to generate 4 permittivity dispersion logs, 4 conductivity dispersion logs, and 1 resistivity log using the two integrated models (Figure 3.1). When $\boldsymbol{S_w}$ and $\boldsymbol{C_w}$ is changed, the integrated model for the proposed joint inversion generates well-defined relative change (relative error with respect to the global minimum) contours that directs the error minimization during the joint inversion (Figure 3.1b & Figure 3.1d). In Figure 3.1a &

Figure 3.1b, the global minimum is at $\boldsymbol{S_w}$= 0.3 s.u. and $\boldsymbol{C_w}$ = 10 S/m because the model output variations are studied for variations in $\boldsymbol{S_w}$ and $\boldsymbol{C_w}$ around $\boldsymbol{m}$=2, $\boldsymbol{n}$=2, $\boldsymbol{C_w}$= 10 S/m, $\boldsymbol{\varphi_t}$ = 0.02, and $\boldsymbol{S_w}$ = 0.3 s.u. The best set of local minima is identified as the dark blue region indicating possible uncertainty in inversion-derived estimates because the minima is spread around the global minimum. It is evident that at low water saturation, the proposed joint inversion (as compared to the integrated SMD and CRI model) shows steeper slope around global minima. In Figure 3.1c & Figure 3.1d, the global minimum is at $\boldsymbol{S_w}$= 0.9 s.u. and $\boldsymbol{C_w}$ = 10 S/m keeping all the other parameters equal to the previous case. At high water saturation, the slopes around global minimum are relatively uniform and flatter compared to the lower water saturation case. A comparison between Figure 3.1a-d indicates that the proposed joint inversion can generate the desired estimates more reliably at low water saturations than at high water saturations.

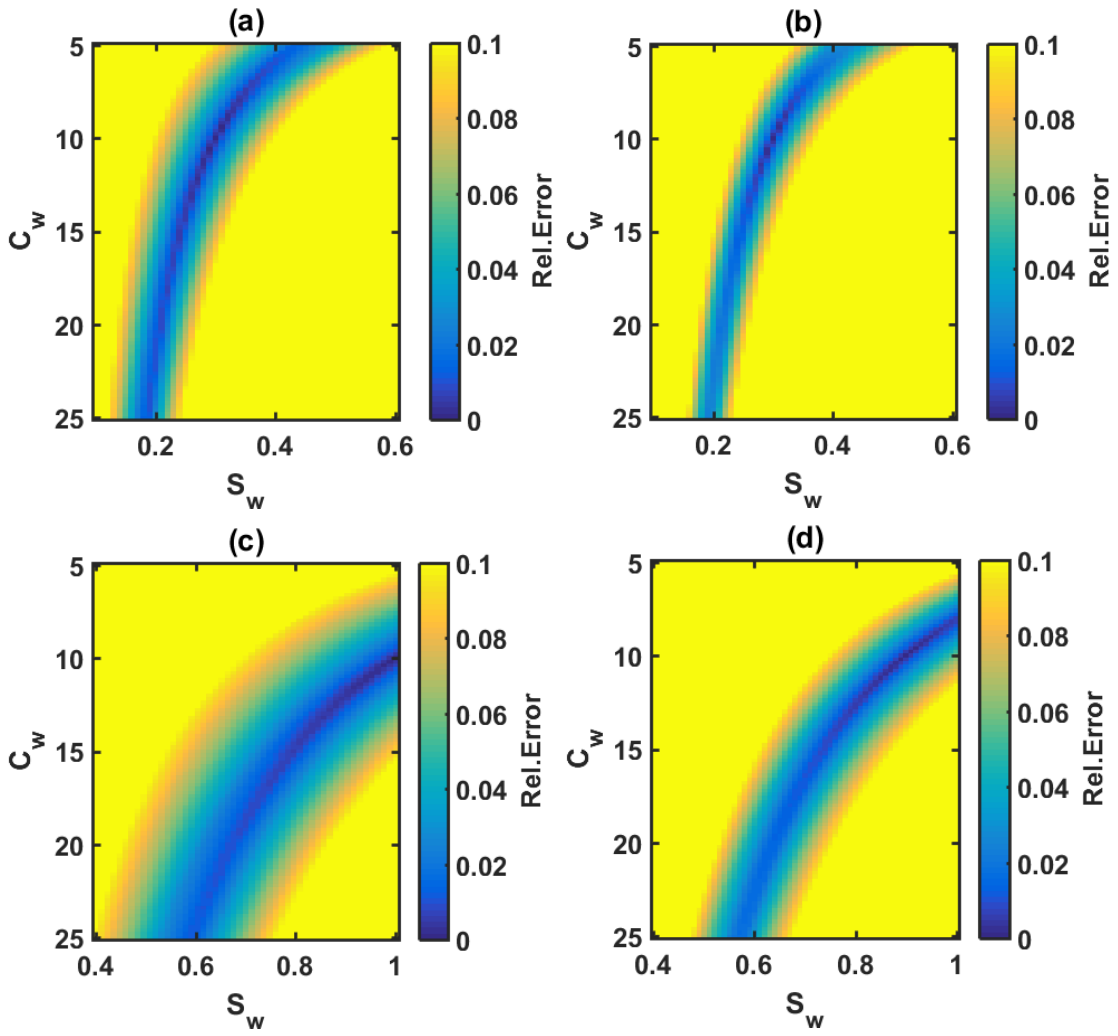

Figure 3.1 Comparison of sensitivity of (a & c) integrated CRIM and SMD model used for dielectric dispersion inversion against that of (b & d) integrated CRIM, SMD and WS model used for the newly proposed joint inversion to variations in S_w and C_w around the default parameters: m=2, n=2, C_w=10 S/m, φ_t=0.02, BQ_v=1.3 mS/cc, and S_w=0.3 s.u. and around the default parameters: m=2, n=2, C_w=10 S/m, φ_t=0.02, BQ_v=1.3 mS/cc, and S_w=0.9 s.u., respectively.

For purposes of model sensitivity comparison critical to understanding the error minimization during the joint inversion, m and n are varied around a default parameter to generate Figure 3.2. The integrated model for the proposed joint inversion with three models generates well-defined error contours around the global minimum that will better direct the error minimization process during the joint inversion compared to those obtained using the integrated CRI and SMD model. A comparison between Figure 3.2a and Figure 3.2b indicates the substantial improvement when

the integrated WS, SMD, and CRI model is implemented instead of the integrated SMD and CRI model. In Figure 3.2a, the spread of errors is very flat around the global minimum that indicates that the error minimization process will not have enough resolution to generate unique results. In Figure 3.2a & Figure 3.2b, the global minimum is at m=2 and n=2 for S_w=0.3 s.u. Figure 3.2c & Figure 3.2d, are generated for a higher saturation of S_w=0.9 s.u., while keeping other parameters of the global minimum similar to the previous case. A comparison between Figure 3.2b and Figure 3.2d indicates that the proposed joint inversion can generate the desired estimates more reliably at low water saturations and the inversion-derived estimates will tend to be non-unique at high water saturations of around 0.9 s.u. This is similar to the observations for variations in S_w and C_w presented in the previous section. Similarly, in this case with increase in water saturation, the sensitivity of the integrated WS, SMD, and CRI model to variation in m is significantly deteriorated while maintaining the sensitivity to variation in n. Deterioration of sensitivity of the integrated model to a specific model parameter indicate increased uncertainty in the corresponding estimates obtained from log processing.

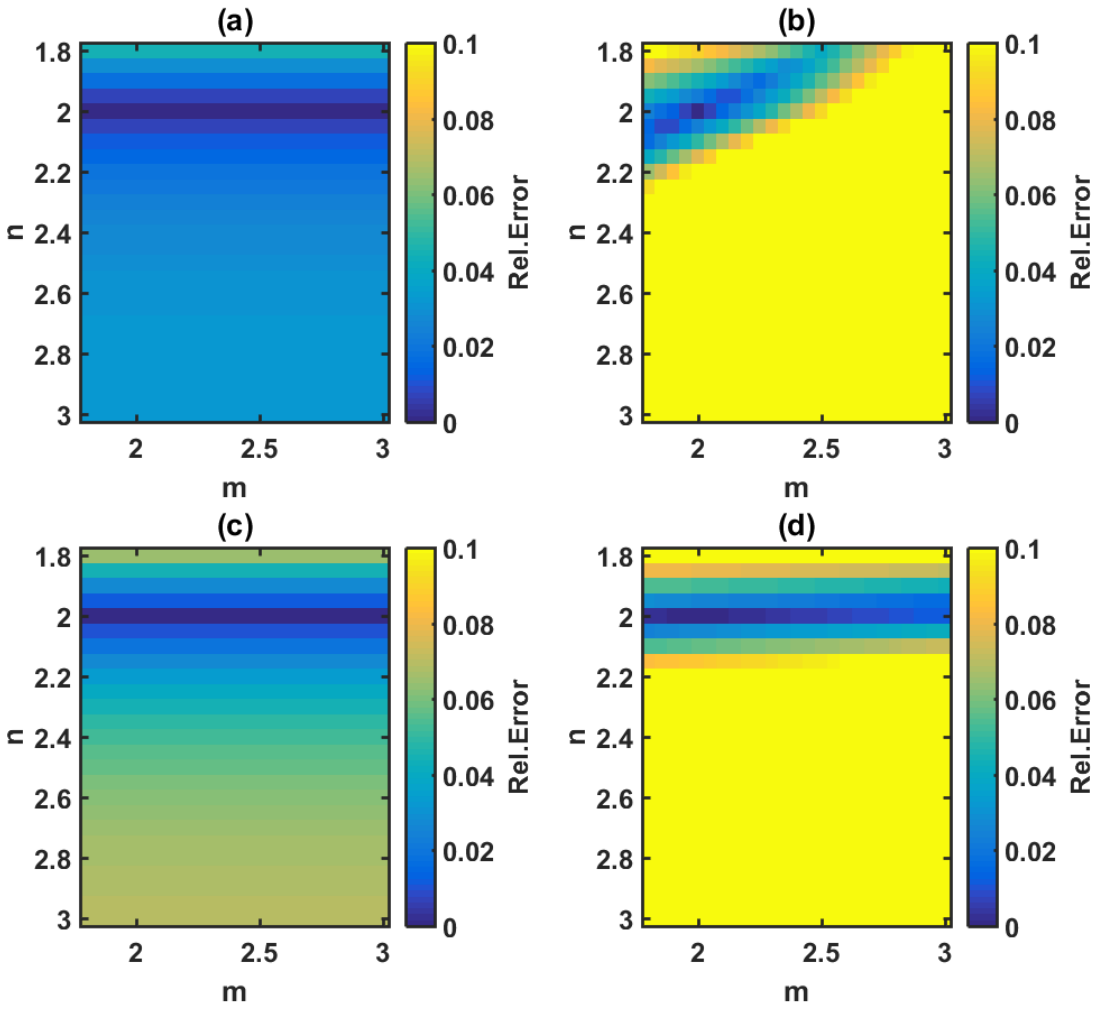

Figure 3.2 Comparison of sensitivity of (a & c) integrated CRIM and SMD model used for dielectric dispersion inversion against that of (b & d) integrated CRIM, SMD and WS model used for the newly proposed joint inversion to variations in n and m around the default parameters: m=2, n=2, C_w=10 S/m, φ_t=0.05, BQ_v=1.3 mS/cc, and S_w=0.3 s.u. and around the default parameters: m=2, n=2, C_w=10 S/m, φ_t=0.05, BQ_v=1.3 mS/cc, and S_w=0.9 s.u., respectively

3.3 Uncertainties in inversion-derived estimates

After demonstrating that the newly proposed joint log processing will perform better compared to processing only the dielectric dispersion logs, we test the sensitivity of the integrated CRIM, SMD and WS model to variations in n and C_w for various S_w. Sensitivity of the integrated model to the petrophysical parameters, in this case n and C_w, is inversely correlated to the uncertainty in the parameter estimation when performing the joint inversion because the model sensitivity directly

affects the error minimization process. In Figure 3.3, global minimum is at default parameters: n = 2 and $C_w = 10$ S/m, identified as the dark blue region. Variations in n and C_w results in change in the relative error of the integrated model response with respect to the response obtained using the default parameters. It is evident from Figure 3.3a-d that with increase in water saturation from 0.2 to 0.99 saturation units (s.u.), the sensitivity of the integrated model to n and C_w decreases. Consequently, the uncertainty in the estimations of n and C_w should increase with increase in water saturation. At S_w=0.9, the joint inversion should generate unreliable non-unique estimates (Figure 3.3c). At high water saturation, the sensitivity of the integrated model decreases more drastically for n in comparison to C_w. To a relatively limited extent, the proposed inversion should estimate C_w more reliably at higher water saturation.

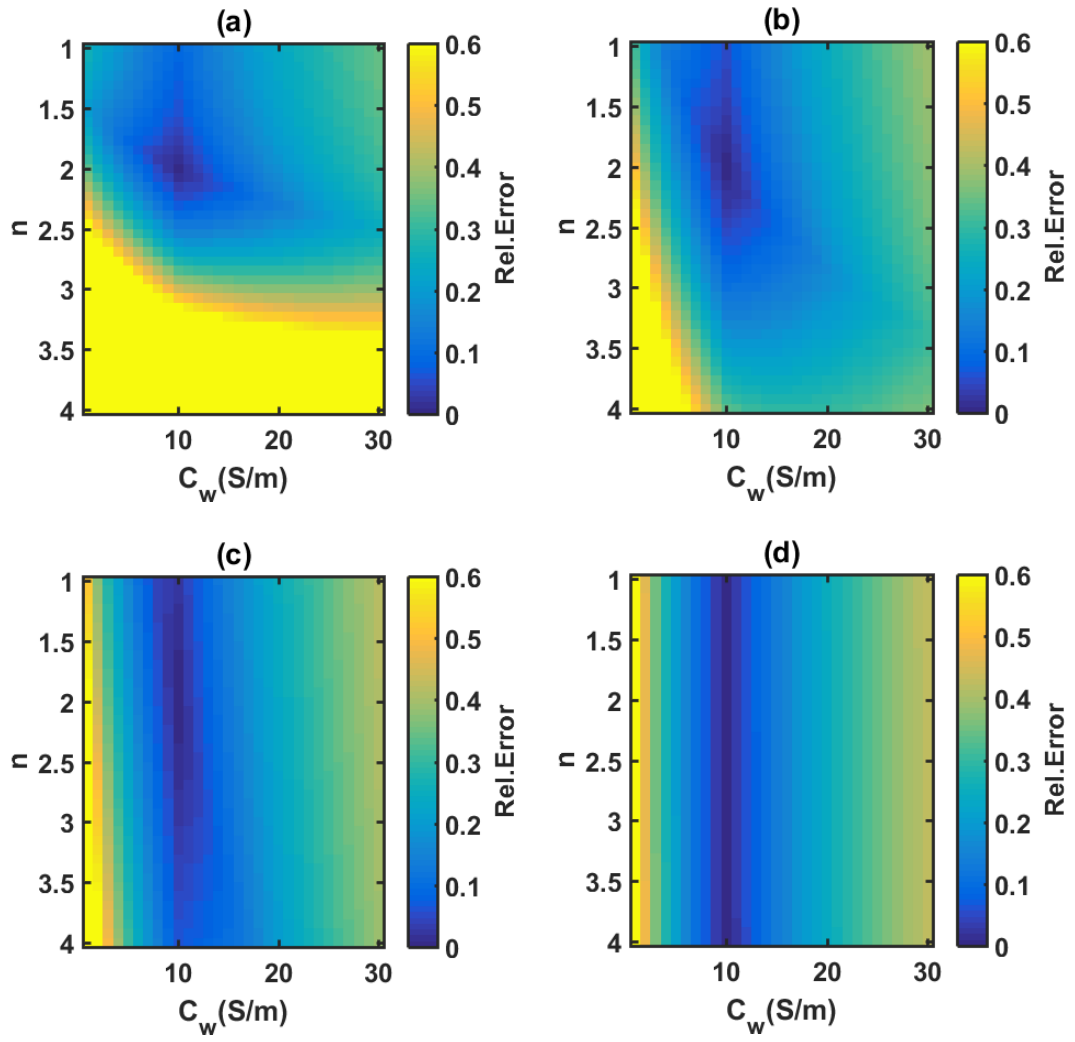

Figure 3.3 Comparison of sensitivities of the integrated CRIM, SMD and WS model to variations in n and C_w for (a) S_w=0.2, (b) S_w=0.5, (c) S_w=0.8, and (d) S_w=0.99 around default parameters: n =2,m=2, φ_t=0.05, C_w=10 S/m, and BQ_v=1.3 mS/cc.

Figure 3.4 illustrates the sensitivity of the integrated model to variations in m and S_w for various S_w. Global minimum is at default parameters: m=2 and S_w=0.9 s.u., identified as the dark blue region in Figure 3.4. It is evident from Figure 3.4a-c that with increase in n from 2 to 4, the sensitivity of the integrated model to m and S_w increases; consequently, the uncertainty in the estimations of m and S_w should decrease. The improvement in sensitivities for the two parameters with increase in n are relatively equal. With increase in C_w (Figure 3.4d), there is a slight

improvement in the model sensitivity to m and S_w, as observed between Figure 3.4a and Figure 3.4d.

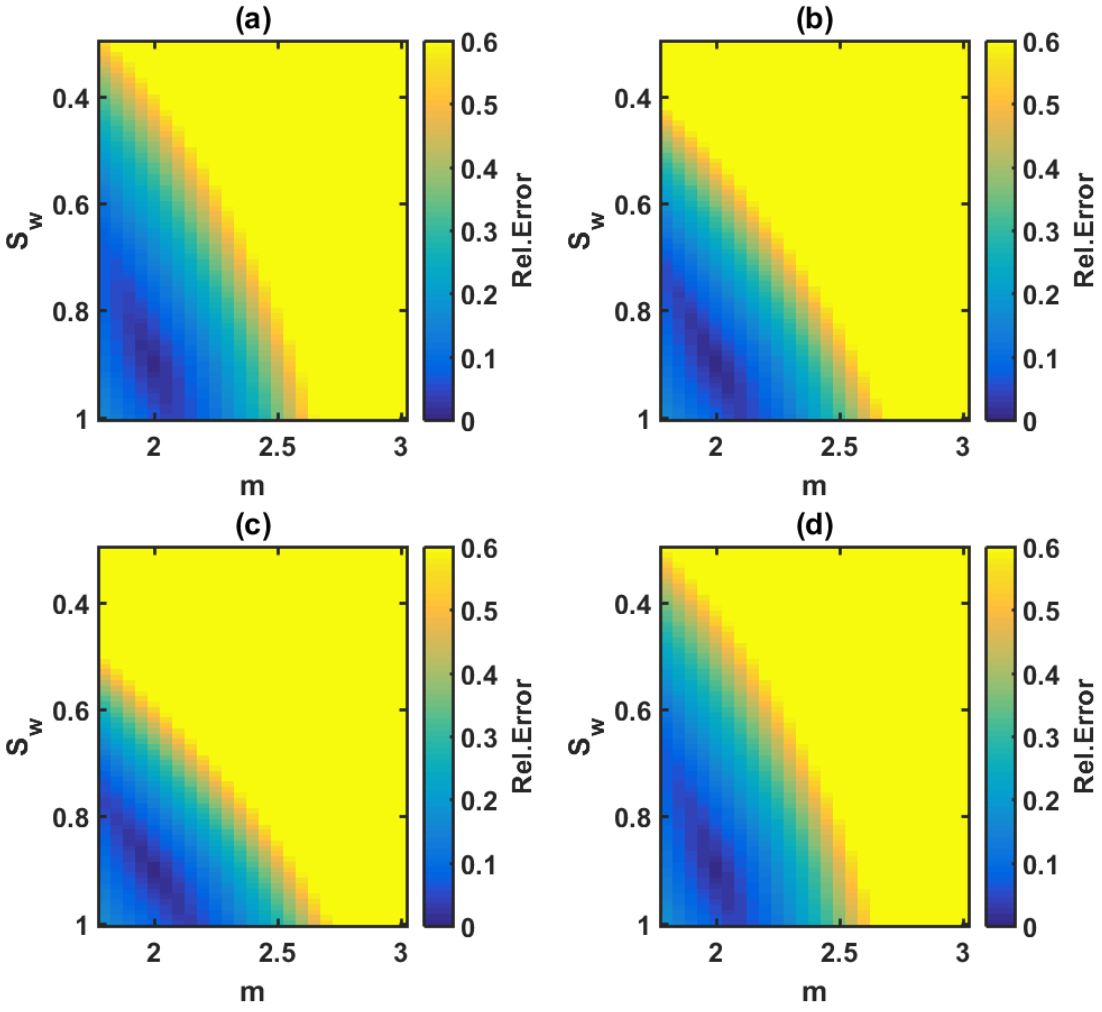

Figure 3.4 Comparison of sensitivities of the integrated CRIM, SMD and WS model to variations in m and S_w for (a) n=2,C_w=10 S/m; (b) n=3,C_w=10 S/m; (c) n=4,C_w=10 S/m; and (d) n=2,C_w=30 S/m around the default parameters: m=2, φ_t=0.05, S_w=0.9 s.u. and BQ_v=1.3 mS/cc.

In Figure 3.5, the global minimum is at φ_t= 0.02 and C_w= 10 S/m for S_w =0.3. When φ_t and C_w are changed, the integrated WS, SMD, and CRI model for the proposed joint inversion generates well-defined error contours (Figure 3.5b) around the global minimum that directs the error minimization during the joint processing of the 9 EM logs. However, when using only SMD and

CRI model to invert only the dielectric dispersion log, the error contour plots exhibit several local minima in Figure 3.5a. The problem of estimate uncertainty increases with increase in water saturation as shown in Figure 3.6. Figure 3.6 shows the error contours when φ_t and C_w are changed around the global minimum of φ_t= 0.02 and C_w = 10 S/m at S_w=0.6. In the Figure 3.5a and Figure 3.6a, the local minima become more prominent and widespread, especially in the case of Figure 3.6a, which indicates a lower sensitivity of the integrated SMD and CRI model for inversion of only the dielectric dispersion logs.

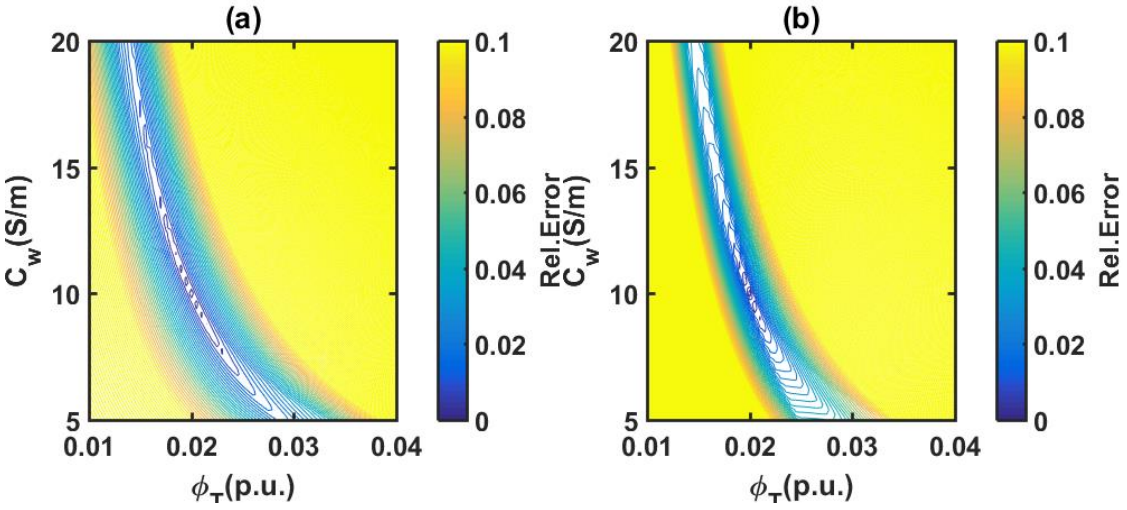

Figure 3.5 Comparison of sensitivity of (a) integrated CRIM and SMD model for dielectric dispersion inversion against that of (b) integrated CRIM, SMD and WS model for the proposed joint inversion to variations in φ_t and C_w around default parameters: $n = 2, m = 2, \varphi_t = 0.02, C_w = 10\ S/m$ and $S_w = 0.3$

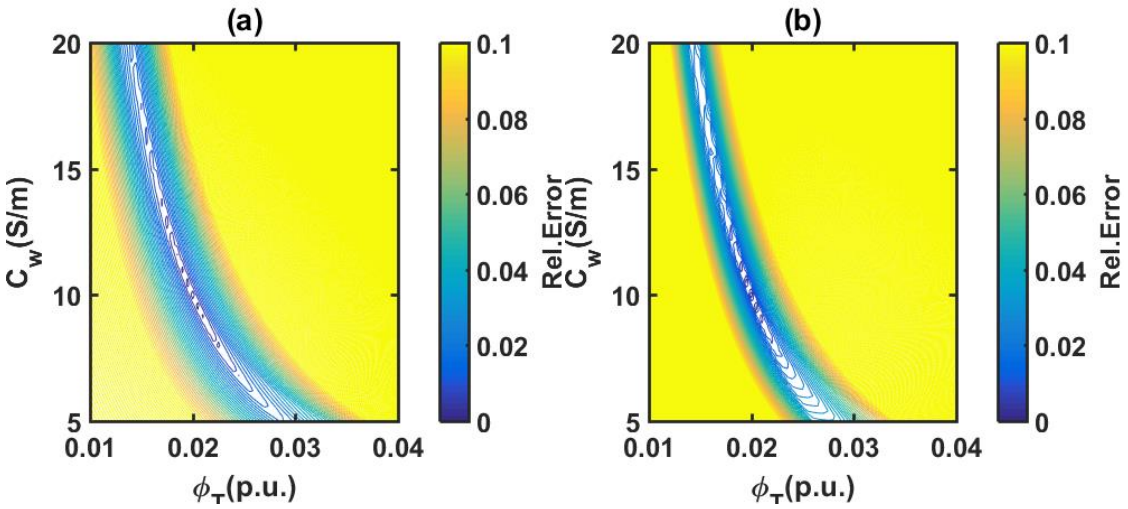

Figure 3.6 Comparison of sensitivity of (a) integrated CRIM and SMD model for dielectric dispersion inversion against that of (b) integrated CRIM, SMD and WS model for the proposed joint inversion to variations in φ_t and C_w around default parameters: $n = 2, m = 2, \varphi_t = 0.02, C_w = 10\ S/m$ and $S_w = 0.6$

3.4 Effect of pyrite in low porosity high salinity formations

Errors in hydrocarbon saturation estimates from EM logs are largest for low-porosity, low-water-saturation, high-salinity formations (Seleznev et al., 2014). Presence of pyrite in the formation leads to the underestimation of hydrocarbon saturation (Clennell et al., 2010), especially when deriving them using dielectric dispersion logs. Concentration of pyrite reduces electrical resistivity of the formation, that is more significant in kHz frequency range (Clavier et al., 1976). In strict terms, SMD model was not developed for clay- and pyrite-rich formations. We analyze the effect of the presence of pyrite in low-porosity high-salinity formation on the proposed joint inversion in comparison to that on the inversion of dielectric dispersion log. To that end, we compare the sensitivity of the two integrated models, one for the proposed joint inversion and the other for the dielectric dispersion inversion, to the variations in S_w and volume fraction of pyrite (V_{py}) in the range of 0% to 10%. In Figure 3.7 and Figure 3.8, the color of the map changes from yellow to dark blue indicating the magnitude of the errors. Comparison of Figure 3.7a & Figure 3.7b

indicates that the integrated CRIM, SMD and WS model used for the proposed joint inversion is more sensitive to variation in volume fraction of pyrite compared to the integrated CRIM and SMD model used for dielectric dispersion inversion. Consequently, the proposed joint inversion is more suited in the presence of pyrite compared to the inversion of dielectric dispersion logs. Based on Figure 3.7b and Figure 3.8b, when initializing the inversion scheme, faster convergence can be achieved by initializing the inversion with a low value of water saturation. Comparison of Figure 3.7b & Figure 3.8b indicates that the sensitivity of the integrated model for joint inversion is relatively invariant to the change in V_{py}.

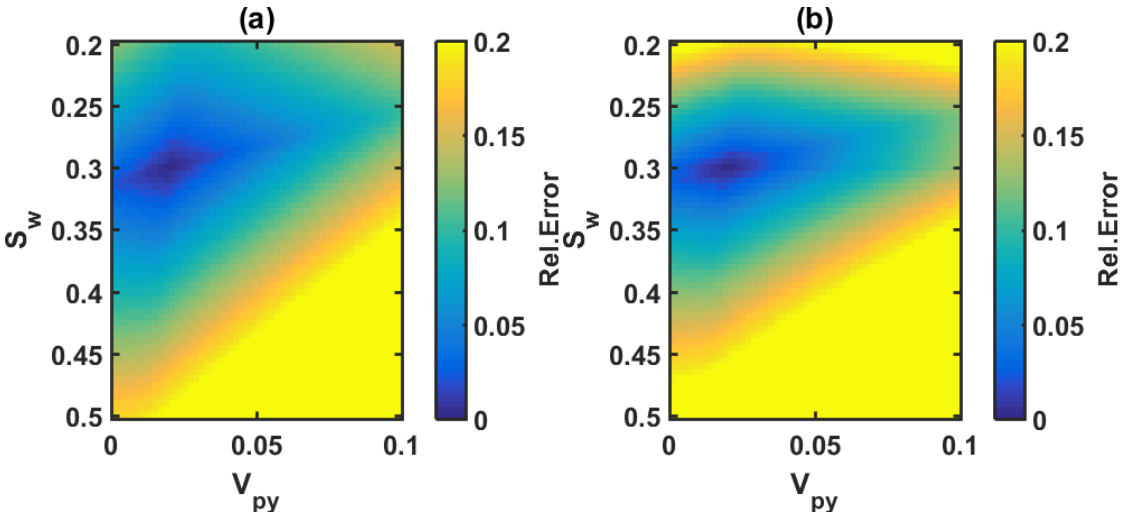

Figure 3.7 Comparison of sensitivity of (a) the integrated CRIM and SMD model used for dielectric dispersion inversion against that of (b) the integrated CRIM, SMD and WS model used for the proposed joint inversion to variations S_w and V_{py} around the default parameters: n=2, m=2, φ_t=0.02, C_w=10 S/m, V_{py}=0.02, BQ_v=1.3 mS/cc, and S_w=0.3 s.u.

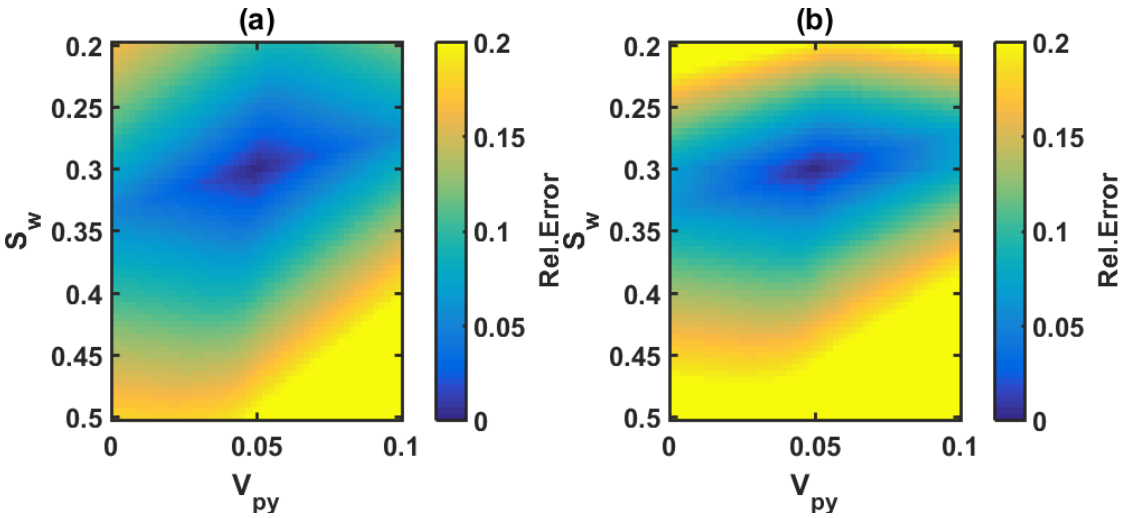

Figure 3.8 Comparison of sensitivity of (a) the integrated CRIM and SMD model used for dielectric dispersion inversion against that of (b) the integrated CRIM, SMD and WS model used for the proposed joint inversion to the variations in S_w and V_{py} around default parameters: n=2, m=2, φ_t=0.02, C_w=10 S/m, V_{py}=0.05, BQ_v=1.3 mS/cc, and S_w=0.6 s.u.

3.5 Threshold of brine conductivity in WS, SMD, and CRI model

As stated earlier, at certain salinity the dielectric measurements lose sensitivity porosity and water saturation. The threshold of brine conductivity is temperature dependent and depends on the brine conductivity rather than salinity. We studied the sensitivity, or the rate of change of resistivity, permittivity and conductivity modeled using the integrated WS, SMD, and CRI model to brine conductivity for the 9 EM log acquisition frequencies. We vary the brine conductivity in the range of 0 S/m to 100 S/m and normalize the derivative plot to generate the 4 permittivity dispersion logs, 4 conductivity dispersion logs, and 1 resistivity log. We analyze three distinct scenarios of water-rich layer of S_w = 0.9 s.u., oil-rich layer of S_w = 0.1 s.u., and clay-rich layer of S_w = 0.9 s.u. and volume of clay V_c = 40% at formation temperature of 230°F (Figure 3.9). It is evident that at high water saturation (Figure 3.9a), the derivative plot for conductivity decreases drastically till 20 S/m and then starts decreasing gradually till 40 S/m. After 40 S/m, the change in derivative plot for conductivity is negligible, which suggests that the model loses sensitivity to brine conductivity

beyond this point. For the derivative plot of permittivity as well, the model loses sensitivity at around 50 S/m. The derivative plot of resistivity decreases drastically till 100 S/m. In comparison to water-rich interval, the oil-rich interval exhibits higher brine conductivity threshold (Figure 3.9b). For clay-rich interval at high water saturation in Figure 3.9c, the results are relatively similar to the water-rich layer (Figure 3.9a). With this study of sensitivity analysis, the upper bound of brine conductivity for purposes of our inversion was chosen to be 45 S/m.

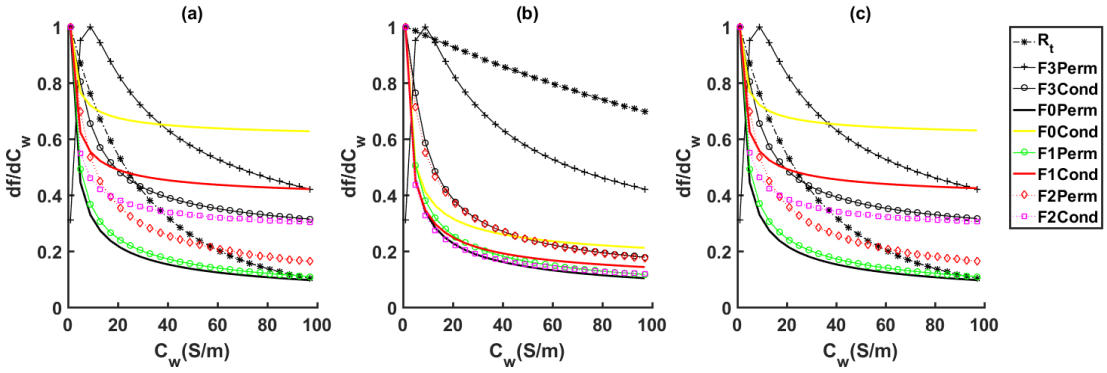

Figure 3.9 Comparison of sensitivity of resistivity at 20 kHz and permittivity and conductivity dispersions at frequencies: F0 (22 MHz), F1 (100 MHz), F2 (350 MHz) and F3 (1 GHz) to brine conductivity for (a) water rich layer of S_w=0.9 s.u. (b) oil-rich layer of S_w=0.1 s.u. and (c) clay-rich layer of S_w=0.9 s.u. and V_c=40% with default parameters m=2, n=2, φ_t=0.07, and BQ_v=75 mS/cc.

3.6 Conclusions

We discussed robustness and sensitivity of the inversion scheme combining dielectric and resistivity logs and compare with only dielectric dispersion logs. Estimates derived from the joint inversion were robust in the presence of pyrite, low water saturation, and low porosity as compared to estimates from the inversion of only four-frequency dielectric dispersion logs. Sensitivity of resistivity, permittivity, and conductivity to brine conductivity is lost for brine conductivity greater than 45 S/m. The proposed joint inversion can generate the desired estimates more reliably at low

water saturations (S_w= 0.3 s.u.) and the inversion-derived estimates tend to be non-unique at high water saturations of around 0.9 s.u.

4. Synthetic Case Study and Field Case Study

4.1 Abstract

Robustness of the parameter estimation could be addressed by synthetic model and the model predictions. We present the application of the newly proposed inversion-based petrophysical interpretation for two formations, Upper Wolfcamp shale formation and Bakken Petroleum System (BPS). Data misfit between modeled and measured parameters provide robustness of our inversion scheme.

4.2 Synthetic Case Histograms and Model Predictions

The uncertainty in parameter estimation when using the proposed joint inversion scheme is studied in this section. 10% Gaussian noise was considered in the synthetic case. The porosity of the formation was selected to be 5% and brine conductivity as 10 S/m to create a synthetic model equivalent to the Upper Wolfcamp formation. Values for other petrophysical properties are listed in Table 4.1. Using these properties, we generated 1 resistivity log at laterolog frequency and 8 permittivity/conductivity dispersion logs at the dielectric tool frequencies. These simulated conductivity, permittivity, and resistivity logs were jointly inverted using the proposed joint inversion coupled with the integrated CRIM, SMD and WS model to estimate C_w, S_w, n, and m of the synthetic formation using a scheme similar to that explained in Section 5 and used by Han and Misra (2017). Inversion-derived estimates of the unknown model parameters, namely C_w, S_w, n, and m, match with the assumed values listed in Table 4.1: Petrophysical parameters assumed for synthetic case study.

Figure 4.1 shows the histogram plot showing the frequency of occurrence of the four inversion-derived estimates for the 250 random initializations of the inversion scheme. For the synthetic case

study, the inversion results show fast and robust convergence to desired values. Relative error in matching the synthetic data using the inversion-derived estimates is 0.01. The good agreement between the synthetic data and the integrated model predictions based on the inversion-derived estimates is illustrated in Figure 4.2. For the 520-ft interval of Upper Wolfcamp formation, no core data was available. The operating company did not retrieve any core samples in this interval. Core water saturation for other layers were available, but they were invaded with the invasion fluid. These water saturation values were very low due to the oil-mud invasion and cannot not be trusted (Tathed et al., 2018a).

Table 4-1: Petrophysical parameters assumed for synthetic case study

Parameters	Values
Total porosity	5%
Volume fraction of clay	25%
Cation exchange capacity (CEC) per unit pore volume, Q_v	0.1 meq/cc
Equivalent conductance of sodium clay exchange cations, B	13 mS/meq
Relative permittivity of hydrocarbon	3.5
Relative permittivity of brine	80
Homogeneity index, α	0.5
Bulk conductivity of brine, C_w	10 S/m
Water saturation, S_w	30%
Cementation exponent, m	2
Saturation exponent, n	2

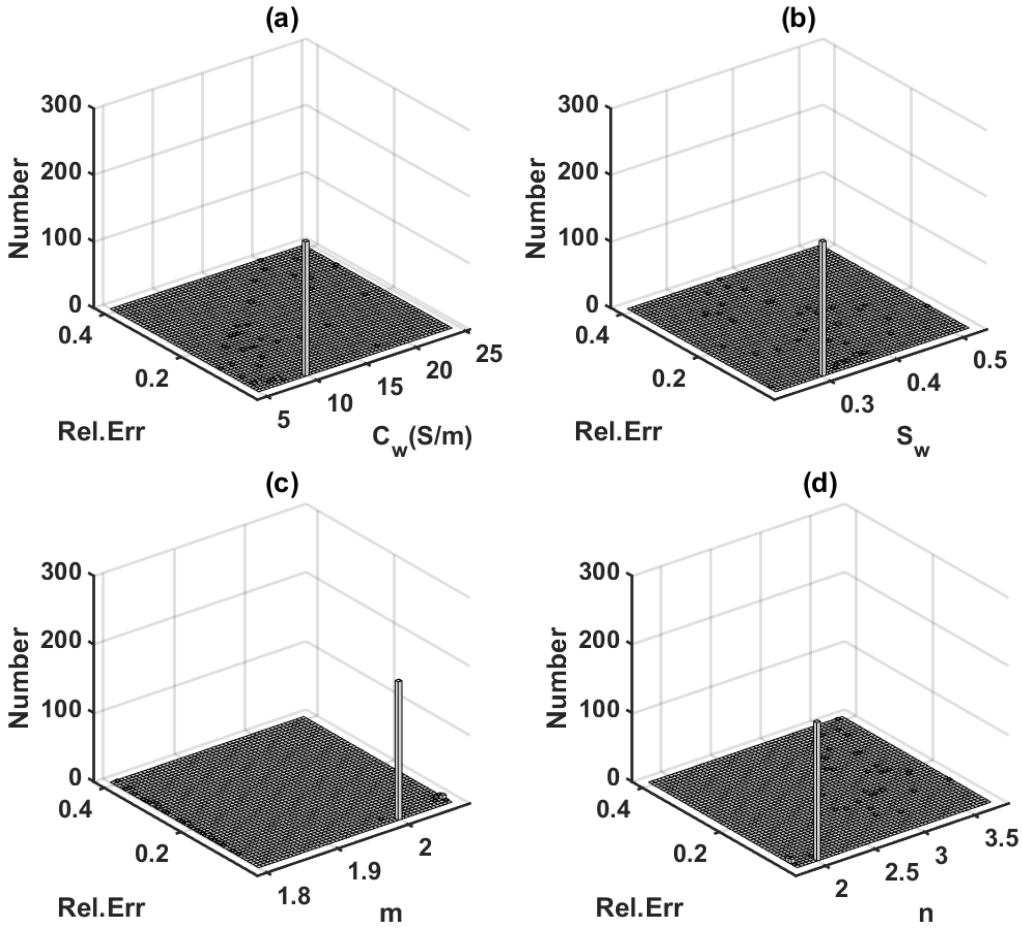

Figure 4.1 Frequency of occurrence of the inversion-derived estimates of (a) C_w, (b) S_w, (c) $m = 2$, and (d) $n = 2$ with relative errors in matching the synthetic data for 250 random initializations of the proposed joint inversion of synthetic data, shown in Figure 4.2.

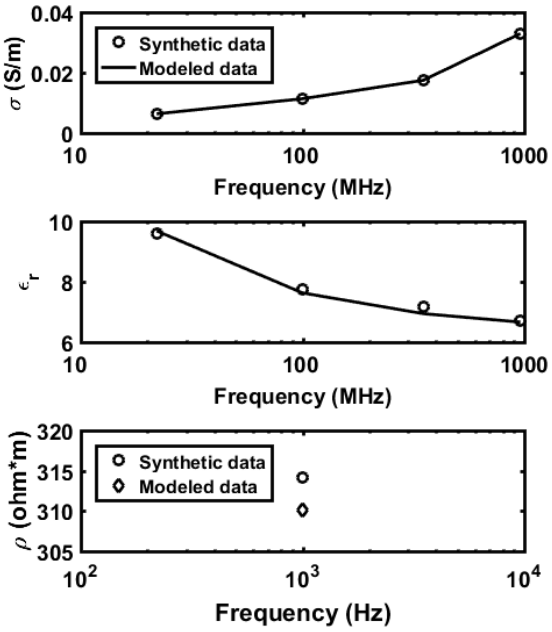

Figure 4.2 Comparison of synthetic effective conductivity, relative permittivity, and resistivity data and the integrated model predictions based on the inversion-derived estimates.

4.3 Field Case Study 1

4.3.1 Wells in Study and Characteristics

The joint inversion scheme was applied to dielectric dispersion and laterolog resistivity logs acquired in a well in upper Wolfcamp shale formation. Upper Wolfcamp comprises mostly of shale, varying from almost black to gray and greenish gray with several interbedded limestone and calcareous sandstone layers. A continuous estimation of Sw, Cw, m, and n was carried out across the 520-ft depth interval in Upper Wolfcamp formation. Unlike conventional interpretation methods, 250 random initializations were performed for each depth to find the global minimum and the range of uncertainties in the estimates. Estimated time required for the proposed inversion method to process the logs acquired from 520-ft depth interval was about 20 hours.

Figure 4.3, Figure 4.4, and Figure 4.5 contain logs of inversion-derived estimates in the Upper Wolfcamp formation. Figure 4.3 represents top part of Upper Wolfcamp formation from XX060-XX130 feet This portion mainly comprises of 60-80% quartz, 10-20% clay and calcite (Track 5) and negligible TOC (total organic carbon). This interval of Wolfcamp formation has low resistivity on the laterologs (<10 ohm.m). There are several laminations and beds exhibiting low porosity (Track 4). These low-porosity streaks are primarily calcite cementation (Track 5). Negligible effect of invasion was observed at different depths of investigation of laterolog resistivity measurements (Track 3). Therefore, we assume that the water saturations sensed by dielectric dispersion logs and resistivity log are equivalent in absence of bed boundaries. With an increase in depth, the Upper Wolfcamp formation mainly consist of tight carbonates (Figure 4.4, XX330-XX360 feet) as calcite content increases (Figure 4.4, track 5). Formation micro-images shows presence of healed, resistive fractures and weak dissolution features in these tight carbonate formations. On triple combo logs, these intervals have low density (<2.55gm/cc) and elevated resistivity (>30 ohm.m). These depths exhibit small pores and tight formations as observed from the (Nuclear Magnetic Resonance) NMR T2 distribution (Track 13, Figure 4.4). With further increase in depth (Figure 4.5), there are thin laminations and interbeds of calcite and clays. Total Organic Carbon (TOC) ranges from 2-3%. There are several streaks of high resistivity, low porosity formations with high calcite deposition. These depths exhibit wide range of pore size distribution as exhibited in Track 13 of Figure 4.5.

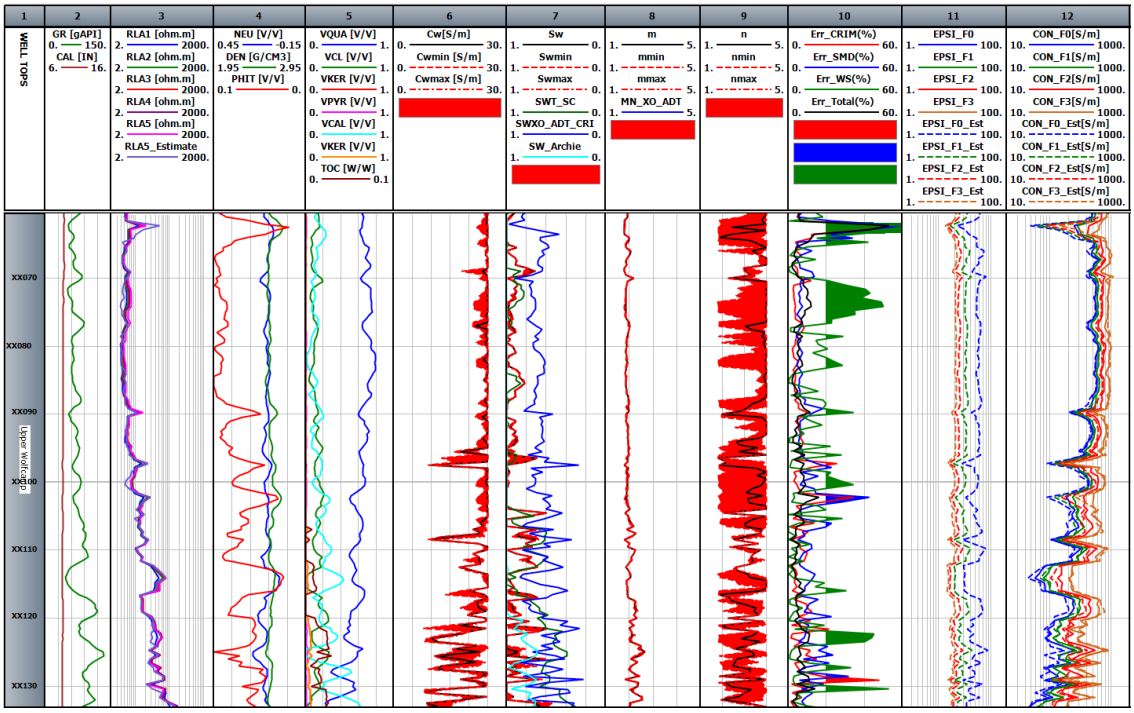

Figure 4.3 Track 1 is the depth (XX060-XX130) and formation type, Track 2 is the gamma ray (GR) and caliper (CAL), Track 3 is the laterolog resistivity (RLA), Track 4 contains the neutron porosity (NEU), bulk density (DEN), and total porosity (PHIT), Track 5 contains volume fractions of various minerals: quartz, chlorite, kerogen, pyrite, and calcite, Track 6 contains inversion-derived brine conductivity (*Cw*) estimate with a range, Track 7 contains water saturation estimated using various methods (*Sw*), Track 8 contains inversion-derived cementation exponent estimate (*m*) estimate with a range, Track 9 contains inversion-derived saturation exponent estimate (*n*) estimate with a range, Track 10 contains relative errors in dielectric and induction model, Track 11 contains measured (bold) and modeled (dash) permittivity dispersion logs at four frequencies, and Track 12 contains measured (bold) and modeled (dash) conductivity logs at four frequencies.

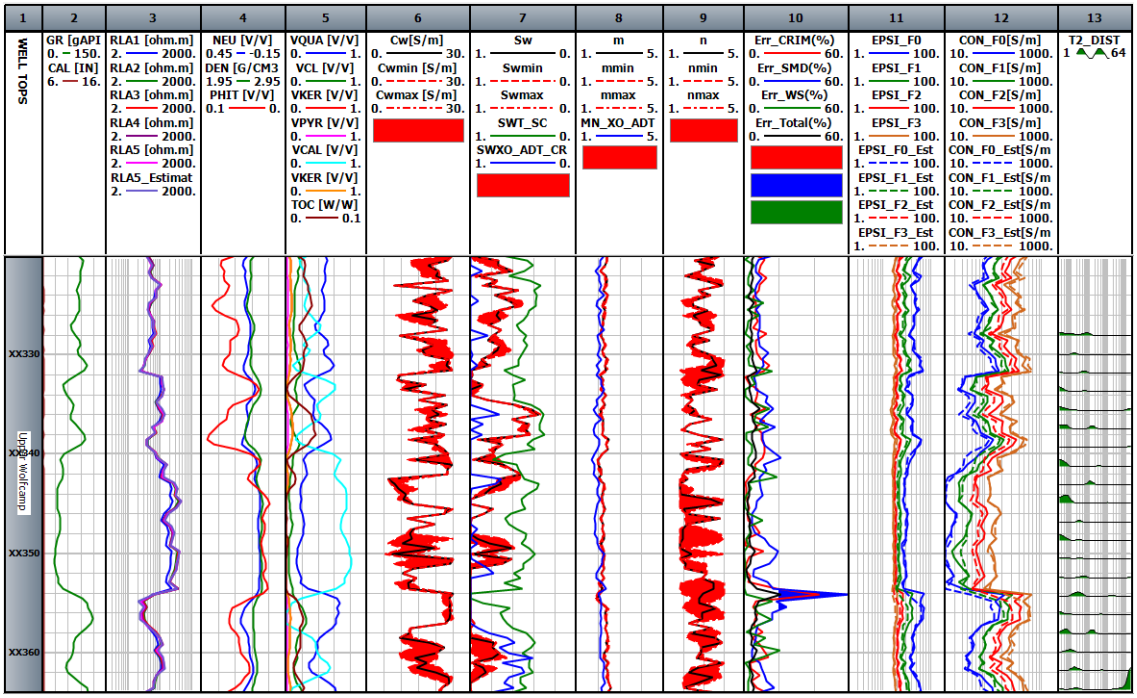

Figure 4.4 Logs for formation depth from XX322 to XX360. The logs and the layout presented in this figure are similar to those in Figure 4.3. Track 13 contains T2 NMR distribution

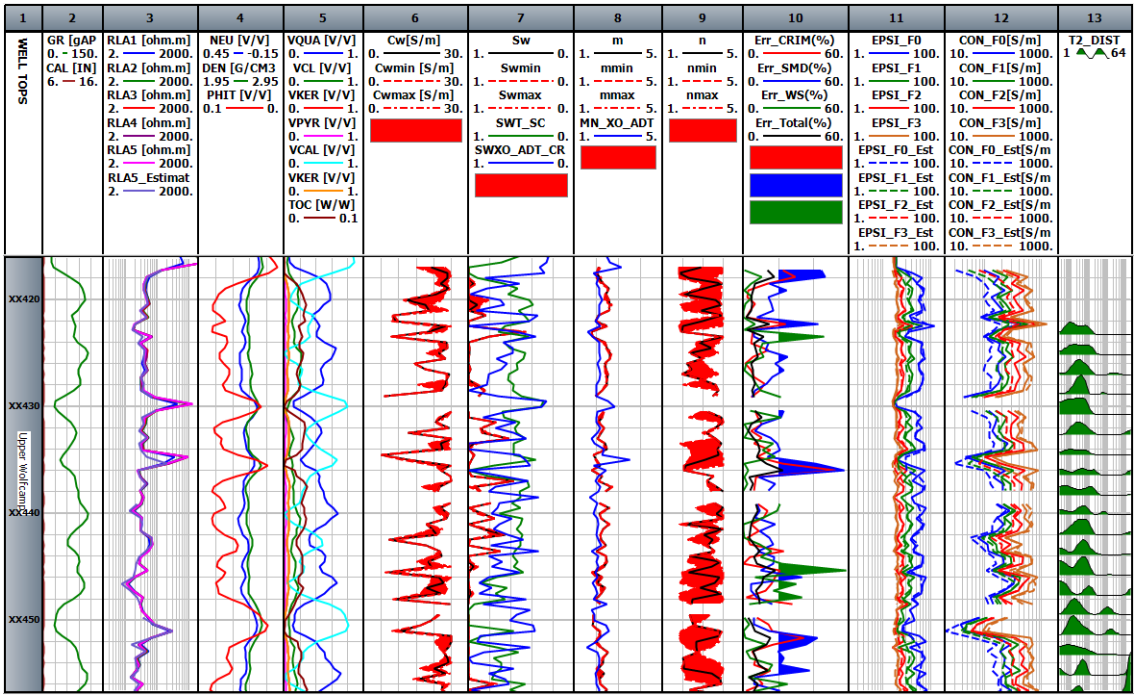

Figure 4.5. Logs for formation depth from XX412 to XX450. The logs and the layout presented in this figure are similar to those in Figure 4.3.

4.3.2 Log interpretation of our estimates

In the depth interval from XX060 to XX130 ft, S_w estimates obtained using the proposed inversion (Figure 4.3, Track 7) are in good agreement with those estimated using the multi-mineral inversion performed by an O&G service company (Figure 4.3). The water saturation estimated by processing low-frequency galvanic/induction resistivity using Archie's equation (Figure 4.3, Track 7, aqua color) indicates that XX060-XX130 is 100%-water bearing zone, whereas only dielectric dispersion logs measured by dielectric tool underestimates water saturation by 25% (Figure 4.3,Track 7, blue color). Inversion-derived S_w estimates are more than 20% higher than those estimated by the service company's multi-mineral inversion for depth intervals XX330-XX360 ft (Figure 4.4) and XX430-XX460 ft (Figure 4.5). Cementation exponent estimates computed using the inversion ranges from 1.8-2.1 and matches with the estimates obtained by the service company, as shown in Track 8 of Figure 4.3. Estimates of cementation exponent obtained using the proposed inversion exhibits higher variations with the increase in depth ranging from 1.8-2.7, as shown in Track 10 of Figure 4.5 in comparison to that of Figure 4.3, that correlates with variations in clay content and porosity. Notably, based on the sensitivity analysis presented in Figure 4.4, uncertainty in saturation-exponent estimates increase with increase in water saturation. Inversion-derived estimates of water saturation are maximum at depth XX098-XX104 feet, and in that depth interval the saturation exponent is the most uncertain. Similar to the sensitivity analysis performed in the earlier sections, water saturation and cementation exponent estimates have higher certainty in comparison to saturation exponent and brine conductivity estimates, as shown in Figure 4.3, Figure 4.4, and Figure 4.5. In Figure 4.4, at depth XX320-XX360 feet, large uncertainty observed in brine conductivity estimates is primarily because the integrated model is not able to account for the polarization mechanism that is resulting in large frequency-dependence of the effective

conductivity measured by the dielectric dispersion tool (Track 12). Uncertainty in C_w estimates in the formation shown in Figure 4.3 is low that correlates with the low frequency-dependence of the effective conductivity logs. Based on the sensitivity analysis, the proposed joint inversion shows unreliable estimates at high water saturation and low brine conductivity. From depth XX330-XX360 feet, uncertainty at high water saturations can be observed. The proposed inversion achieves high certainty for the estimates of water saturation, brine conductivity and cementation exponent from depth XX060-XX100 feet. This is a consequence of low clay content and high porosity in that depth interval. Our estimates of brine conductivity and water saturation are uncertain in tight calcareous formations from XX330-XX360 feet. These unreliable estimates could be due to small pores and low porosity beds in that depth interval.

4.3.3 Error Analysis

Data misfit is calculated as the difference between the modeled and measured dielectric dispersion and resistivity logs. The logs are modeled based on inversion-derived estimates obtained using the proposed inversion scheme coupled with the integrated WS, SMD, and CRI model. Data misfit averaged over the 1 resistivity, 4 conductivity, and 4 permittivity logs is reported as the mean relative error, which is expressed as

$$Error_{Total} = \left[\frac{Error_{SMD} + Error_{CRI} + Error_{WaxmanSmits}}{5}\right], \quad (4.1)$$

such that

$Error_{CRI} =$

$$\frac{\left[\frac{abs(Perm^{meas,1GHz} - Perm^{mod,1GHz})}{Perm^{meas,1GHz}} + \frac{abs(Cond^{meas,1GHz} - Cond^{mod,1GHz})}{Cond^{meas,1GHz}}\right]}{2} 100\% \quad (4.2)$$

$$Error_{SMD} =$$

$$\sum_{i=0}^{2} \frac{\left[\frac{abs(Perm^{meas,f_i} - Perm^{mod,f_i})}{Perm^{meas,f_i}} + \frac{abs(Cond^{meas,f_i} - Cond^{mod,f_i})}{Cond^{meas,f_i}}\right]}{6} 100\% \quad (4.3)$$

$$Error_{WS} = \frac{abs(Res_{mod,1kHz} - Res_{meas,1kHz})}{Res_{meas,1kHz}} 100\% \quad (4.4)$$

Error in fitting the conductivity and permittivity logs acquired at 1GHz using the CRI model predictions is referred as the $Error_{CRI}$. Error in matching the 3 conductivity and 3 permittivity dispersion logs acquired at 20, 100 and 260 MHz, respectively, using the SMD model predictions is referred as $Error_{SMD}$. Finally, the error in fitting the resistivity laterolog using Waxman-Smits model predictions is referred as $Error_{WS}$. Track 10 in Figure 4.3, Figure 4.4, and Figure 4.5 contain the various data misfits in matching the corresponding logs with CRI model, SMD model and WS model predictions. In Figure 4.3 Track 10, the depth interval XX060-XX080 exhibits large error due to data misfit in modeling the laterolog resistivity, which on an average range around 40%. This interval exhibits low resistivity and high porosity formation with large volume fraction of quartz; these three characteristics correlate with zones where the $Error_{WS}$ is large. Volume of clay is low in these formations and high $Error_{WS}$ may be a consequence of the assumed

value of 1.3 for BQ_v for the entire formation. In Figure 4.4, depth interval XX343-XX354 feet, shows highest interval of low porosity at an average of 2.5 porosity units. Error in fitting laterolog resistivity log ($Error_{WS}$) and that in fitting the highest-frequency dielectric log ($Error_{CRI}$) is lowest in this interval. Error in fitting the three lowest-frequency dielectric dispersion logs ($Error_{SMD}$) has the highest value in this interval. At the depth XX353.5 feet, $Error_{SMD}$ is about 60% along with $Error_{WS}$ attaining a large value of 50%, which might be a consequence of thin laminations and sand-shale bed boundary effects at that depth. High errors are also observed at XX418, XX436 and XX452 feet in Figure 4.4 due to the errors in SMD and CRIM models. These large errors could be because the integrated model is not able to account for the polarization mechanism that gives rise to a large frequency-dependence of the effective conductivity measured by the dielectric dispersion tool.

4.4 Field Case Study 2

4.4.1 Wells in Study and Characteristics

The joint inversion scheme was applied to dielectric dispersion and induction resistivity logs acquired in a well in Bakken Petroleum System (BPS) for a continuous 350 ft interval (Tathed et al., 2018b). Unlike conventional interpretation methods, 250 random initializations were performed for each depth to find the global minimum and the ranges of uncertainties for the inversion-derived estimates. Estimated time required for the proposed inversion method to process the logs acquired from 350-ft depth interval was about 15 hours.

Figure 4.7 contain logs of inversion-derived estimates in the Lodgepole formation from XX610-XX670 ft. This portion is mainly comprised of 70-80% limestone with 2-3 % porosity (Track 5&6). These low-porosity streaks are primarily calcite cementation (Track 6). Negligible effect of invasion was observed at different depths of investigation of induction resistivity measurements

(Track 4). Therefore, we assume that the water saturations sensed by dielectric dispersion logs and resistivity log are equivalent with the assumption that bed boundaries do not exist in the formation under investigation. Vertical resistivity R_v is higher than horizontal resistivity R_h and the resistivity measured by induction tool (Track 4). Anisotropy is computed in terms of ratio of vertical resistivity R_v and horizontal resistivity, R_h. Lodgepole formation has anisotropy values ranging from 6-9 calculated by R_t scanner (Track 7). These depths exhibit small pores and tight formations as observed from the NMR T2 distribution (Track 15).

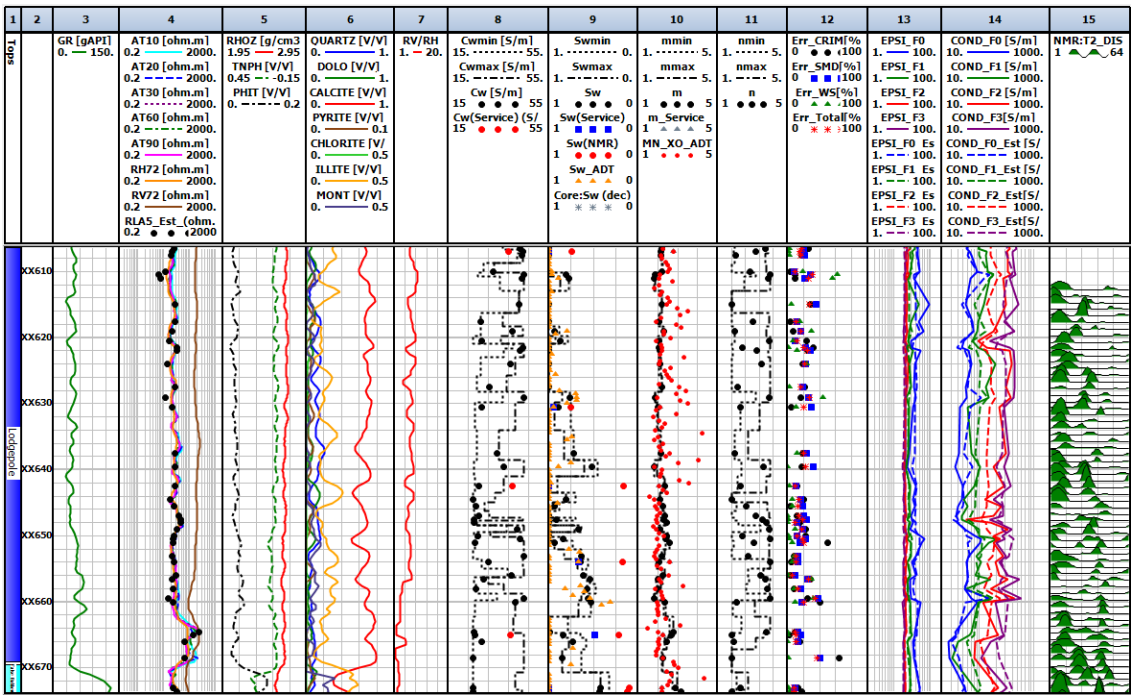

Figure 4.7 Track 1 is the formation type, Track 2 is the depth (XX610-XX670 ft), Track 3 is the gamma ray (GR), Track 4 contains the induction resistivity (AT), horizontal resistivity R_h, vertical resistivity R_v and modeled resistivity , Track 5 contains the bulk density (RHOZ), neutron porosity (TNPH), and total porosity (PHIT), Track 6 contains volume fractions of various minerals: quartz, dolomite, calcite, pyrite, chlorite, illite and montmorillonite, Track 7 contains anisotropy logs derived from R_t scanner, Track 8 contains inversion-derived brine conductivity (C_w) estimate with a range, Track 9 contains water saturation estimated using various methods (S_w), Track 10 contains inversion-derived cementation exponent estimate (m) estimate with a range, Track 11 contains inversion-derived saturation exponent estimate (n) estimate with a range, Track 12 contains relative errors in dielectric and induction model, Track 13 contains measured (bold) and modeled (dash) permittivity dispersion logs at four frequencies, Track 14 contains measured (bold) and modeled (dash) conductivity logs at four frequencies, and Track 15 contains NMR T2 distribution.

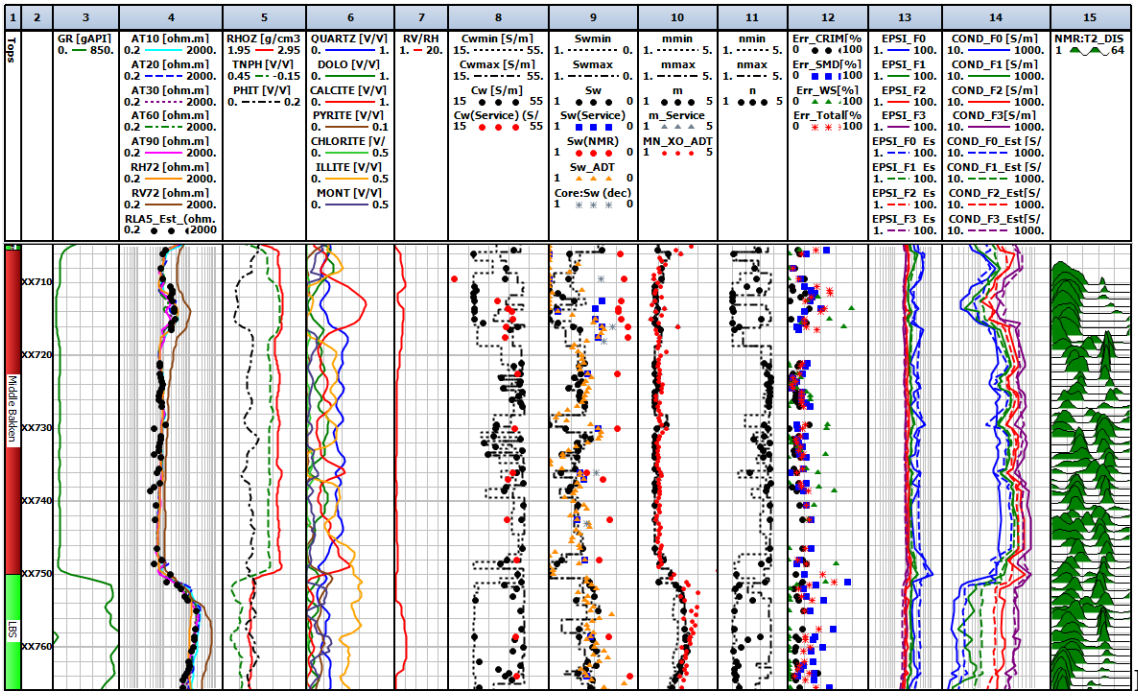

Figure 4.8 Logs for formation interval from the depth of XX710 to XX766 ft. The logs and the layout presented in this figure are similar to those in Figure 6.6.

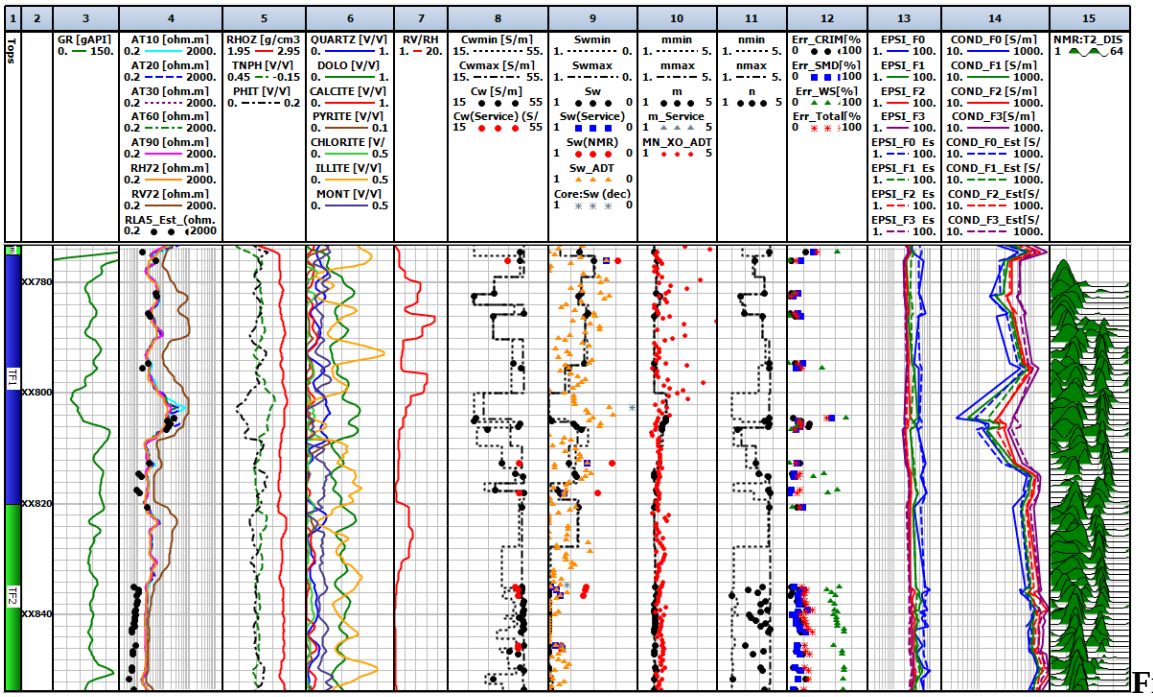

Figure 4.9 Logs for formation interval from the depth of XX780 to XX850 ft. The logs and the layout presented in this figure are similar to those in Figure 6.6.

4.4.2 Log interpretation of our estimates

Figure 4.8 denotes complex reservoir interval of Middle Bakken from XX705.5-XX750 ft and Lower Bakken Shale from XX750-XX766 ft. Lower Bakken shale source rocks are characterized by high volume of clay about 30-40% and pyrite content about 1-3% (Figure 4.8, Track 6). High gamma ray (Figure 4.8, Track 3) is associated with the high TOC and high kerogen content in this formation. Middle Bakken shows range of grain size and sorting from poorly sorted argillaceous siltstone to moderately well sorted fine-grained sandstone (Pirie et al., 2016). Upper Middle Bakken contains well-sorted, fine grained sandstone that marks best reservoir quality. The vertical resistivity R_v in the upper Middle Bakken (XX705.5-XX720 ft) has higher resistivity than horizontal resistivity, R_h and resistivity measured by induction tool (Track 4). Anisotropy value calculated by R_t scanner is around 4 (Track 7). Further in the Middle Bakken, from XX720-XX750 ft, negligible anisotropy is observed. Middle Bakken has highly conductive formations as compared to Lodgepole formation (Track 14). Wide range of pore size distribution is illustrated in Middle Bakken (Track 15). With an increase in depth, Three Forks formation mainly consist of dolostone (40-60%), interbedded with clay rich dolo-mudstone (Figure 4.9 track 6). The uppermost sequence, Three Forks 1 (TF1) denotes the oil-bearing interval in Three Forks from XX775-XX820 ft. The petrophysical analysis of Three Forks formation is mainly complex due to presence of thin beds characterized by high vertical resistivity (Track 4) and anisotropy values as high as 15 (Track 7). At the depth interval XX630.5 and XX654 ft, S_w estimates obtained using the proposed inversion (Figure 4.7, Track 9) are in good agreement with those estimated using the multi-mineral inversion performed by an O&G service company and measured by dielectric ADT tool (Figure 4.7). Inversion-derived S_w estimates are more than higher than those estimated by the NMR log interpretation. Cementation exponent estimates computed using the inversion matches

with the estimates obtained by the service company, as shown in Track 10 of Figure 4.7. In Figure 4.7, at depth XX610-XX670 ft, large uncertainty observed in brine conductivity estimates (Track 8) is primarily because the integrated model is not able to account for the polarization mechanism that results in large frequency-dependence of the effective complex permittivity measured by the dielectric dispersion tool (Track 14). Uncertainty in saturation-exponent estimates increase with increase in water saturation from depth interval XX610-XX628 ft. These unreliable estimates could be due to small pores and low porosity beds in that depth interval. Water saturation and cementation exponent estimates have higher certainty in comparison to saturation exponent and brine conductivity estimates, as shown in Figure 4.7, Figure 4.8, and Figure 4.9. In the Figure 4.8, from depth interval XX705.5-XX720 ft, uncertainties for water saturation and brine conductivity are large which could be due to low porosity (Track 5) and low salinity (Track 14) in this formation. Further in the Middle Bakken from depth XX720-XX750 ft, S_w estimates obtained using the joint inversion (Figure 4.8, Track 9) gets better agreement with those estimated by service company and measured by dielectric ADT tool than Dean-Stark core water saturation (Figure 4.8). Inversion-derived C_w estimates are also in good agreement than those estimated by the service company (Track 8). The proposed inversion achieves high certainty in this interval for the estimates of S_w, C_w, m, and n. This is a consequence of low clay content and high porosity in that depth interval. The reduced uncertainty of the estimates could also be due to lower anisotropy in this depth interval. There is a good agreement between S_w estimates obtained using the proposed inversion (Figure 4.9, Track 9) and those estimated using multi-mineral inversion performed by service company. There is high uncertainty in brine conductivity and saturation exponent in Three Forks 2 formation from XX820-XX850 ft (Figure 4.9, Track 8 and Track 11). This could be the result of large frequency dependence of effective complex permittivity measured by the ADT tool.

4.4.3 Error Analysis

Data misfit is calculated as the difference between the modeled and measured dielectric dispersion and resistivity logs. Data misfit calculations are represented in Equation 6.1, 6.2, 6.3, and 6.4. Error in fitting the conductivity and permittivity logs acquired at 1 GHz using the CRI model predictions is referred as the $Error_{CRI}$. Error in matching the 3 conductivity and 3 permittivity dispersion logs acquired at 22, 100 and 350 MHz, respectively, using the SMD model predictions is referred as $Error_{SMD}$. Finally, the error in fitting the resistivity induction using Waxman-Smits model predictions is referred as $Error_{WS}$. Track 12 in Figure 4.7, Figure 4.8, Figure 4.9 contain the various data misfits in matching the corresponding logs with CRI model, SMD model and WS model predictions. In Figure 4.7, depth XX610 exhibits largest error due to data misfit in modeling induction resistivity, which is about 60%. The anisotropy value reported at this depth is about 9.67 (Track 7). Track 4 resistivity track also shows the presence of thin beds at this depth, due to high vertical resistivity at this depth. The depth interval XX835-XX853.5 in Figure 4.9 exhibits highest error for modeling induction resistivity on an average of around 60%. This interval characterizes low resistivity and large volumes of illite. This high error could also be the result of calculated cationic exchange capacity values in this depth interval. Error in fitting the three low-frequency dielectric dispersion logs ($Error_{SMD}$) has the highest value in this interval. At the depth interval XX750-XX766.5 ft, $Error_{SMD}$ is about 70% along with $Error_{CRI}$ attaining a large value of 35%, which might be a consequence of high pyrite content in that depth interval. SMD and CRIM model fails in high volume of pyrite. In Figure 4.7, the depth interval XX720-XX730 feet exhibits lowest data misfit, in modeling the induction resistivity and dielectric dispersion, which is less than 20%. Such low errors could be due to negligible anisotropy and low pyrite content in this depth interval.

4.5 Limitations of our work

The joint inversion assumes that the volumes sensed by the 8 dielectric dispersion logs at the four frequencies and that sensed by the laterolog resistivity have similar petrophysical properties. This assumption requires the formation to be free from fractures and beds/laminations thinner than 2 feet. Vertical resolution refers to the thinnest bed the tool can accurately sense without the bed-boundary effects. Dielectric tool generally has about 2-inch vertical resolution and 3-inch depth of investigation, whereas laterolog resistivity generally has vertical resolution of 2 ft and depth of investigation of 5 ft. The pad-based micro-resistivity measurements in the 520-ft depth interval of the upper Wolfcamp shale indicate that there are few depths consisting of beds as thin as 0.1 feet. Notably, the use of total porosity for log-processing agrees with the physics of dielectric dispersion tool measurement; however, the use of total porosity will generate erroneous results for galvanic resistivity measurements when isolated pores are present. The integrated model technique assumes that the reservoir volumes sensed by the 8 dielectric dispersion logs at the four frequencies and that sensed by the induction resistivity have similar petrophysical properties. This assumption requires the formation to be free from filtrate invasion, fractures and beds/laminations thinner than 2 feet. Vertical resolution refers to the thinnest bed the tool can accurately sense without the bed-boundary effects. Dielectric tool generally has about 2-inch vertical resolution and 3-inch depth of investigation, whereas induction resistivity generally has vertical resolution of 2 ft and depth of investigation of 8 ft. Another simplification required cationic exchange capacity to be calculated from the clay types and volumetric concentrations of clay minerals. Laboratory experimentation is necessary for more reliable values of cationic exchange capacity. Also, the use of total porosity for log-processing agrees with the physics of dielectric dispersion tool measurement; however, the

use of total porosity will generate erroneous results for galvanic resistivity measurements when isolated pores are present.

5. Conclusions

We successfully processed 8 dielectric permittivity and conductivity dispersion logs (10 MHz – 1 GHz) and 1 laterolog resistivity (~1 kHz) acquired in 520-feet depth interval of the clay- and carbonate-rich Upper Wolfcamp formation. In doing so, a continuous estimation of water saturation, brine conductivity, cementation exponent (textural index), and saturation exponent with ranges of possible values were obtained for the upper Wolfcamp formation. The proposed log processing technique is robust compared to processing only the dielectric dispersion logs, especially in pyrite-rich, low-porosity, and hydrocarbon-bearing formations. The goal is to obtain convergence, which is reached when the estimates do not alter with more iterations. These estimates have higher certainty and better convergence at lower water saturation, which is desired feature of the processing technique. Compared to the estimates for saturation exponent and brine conductivity, water saturation and cementation exponent estimates exhibit higher certainty. Water saturation estimates obtained using the proposed inversion are in good agreement with those estimated using service company's multi-mineral inversion performed in the depth interval from XX060 to XX130 ft, whereas water saturation estimates from Archie's equation interprets 100% water bearing zone. Inversion-derived water saturation estimates are more than 20% higher than those estimated by the multi-mineral inversion for depth intervals XX330-XX360 ft and XX430-XX460 ft. Estimates of cementation exponent obtained using the proposed inversion exhibit higher variation with the increase in depth indicating an increase in heterogeneity/layering with depth. Hydrocarbon saturation in the interval XX334-XX346 ft is close to 30%. There are thin-layers in the interval XX412-XX444 ft having hydrocarbon saturation close to 20%. Hydrocarbon-bearing formation has estimated connate water conductivity of 20 S/m. The saturation exponent estimates

are close to 2.8 in the hydrocarbon-bearing layers and tends to exhibit large uncertainty in the non-reservoir sections of the upper Wolfcamp shale.

The proposed joint interpretation technique processed 8 dielectric permittivity and conductivity dispersion logs (22 MHz – 960 MHz) and 1 induction resistivity (~20 kHz) logs acquired in 350-ft depth interval of the Bakken Petroleum System (BPS). In doing so, continuous estimations of water saturation, brine conductivity, cementation exponent (textural index), and saturation exponent were computed with associated uncertainties in the estimates. Sensitivity of resistivity, permittivity, and conductivity to brine conductivity is lost for brine conductivity greater than 45 S/m. With the estimates of joint inversion technique, water saturation and cementation exponent estimates exhibits less uncertainty as compared to the estimates for saturation exponent and brine conductivity. Water saturation and brine conductivity estimates are most certain in the depth interval XX720-XX750 ft of Middle Bakken, where the formation exhibits high porosity, low clay content, and low anisotropy. Hydrocarbon saturation in this interval is close to 35%. Hydrocarbon saturation close to 60% exists in the 45-ft depth interval of Middle Bakken formation. Anisotropic Three Forks 1 formation, a 40-ft depth interval in the lower section of Bakken Petroleum System, exhibits hydrocarbon saturation close to 40%. Hydrocarbon saturation estimates in Lodgepole formation ranges from 10% to 50%.

Inversion-derived brine conductivity estimates are most uncertain in XX610-XX670 ft interval of Lodgepole formation due to limitation of the integrated model in accounting for the polarization mechanism. High uncertainty in brine conductivity and saturation exponent in Three Forks 2 formation (XX820-XX850 ft) could be due to large frequency dependence of effective complex permittivity, primarily due to the presence of conductive minerals and other unaccounted polarization mechanisms. Depth interval XX720-XX730 feet in Middle Bakken formation shows

less than 20% data misfit in matching induction resistivity and dielectric dispersion due to negligible anisotropy and pyrite content. Depth interval XX835-XX853.5 ft in Three Forks 2 formation exhibits highest data misfit of 60% for induction resistivity. Data misfit in matching dielectric dispersion logs is highest in the depth interval XX750-XX766.5 ft that range from 35% to 75% primarily due to high pyrite content.

As stated earlier, the proposed inversion work assumes that formation should be free from beds less than 2 feet. These thin beds are bypassed due to our limitation of vertical resolution and hence could lead to significant under estimation of our results. For future work, we would recommend analyzing these thin beds. Thomas-Stieber approach could be used for thin bed analysis and calculating parameters like total porosity. For the experimental work, dielectric measurements could be conducted on shale samples over a range of frequencies to characterize electrical properties of shale and relate the responses to other petrophysical properties. Resistivity measurements could be further conducted at different saturation state and different salinity to develop a resistivity-saturation-porosity relationship for organic-rich shales.

References Cited

Archie, G. E., 1942, The Electrical Resistivity Log as an Aid in Determining Some Reservoir Characteristics, Society of Petroleum Engineers, 146,54-67. doi:10.2118/942054-G

Brovelli, A., & Cassiani, G., 2008, Effective permittivity of porous media: A critical analysis of the complex refractive index model, Geophysics Prospecting, 56(5), 715–727

Chan, C.Y., & Knight, R.J., 1999, Determining water content and saturation from dielectric measurements in layered materials, Water Resources Research, 35(1), 85 – 94

Chen, H., & Heidari, Z., 2014, Assessment of Hydrocarbon Saturation in Organic-Rich Source Rocks Using Combined Interpretation of Dielectric and Electrical Resistivity Measurements, SPE Annual Technical Conference and Exhibition, Society of Petroleum Engineers. doi:10.2118/170973-MS

Clavier, C., Heim, A., & Scala, C., 1976, Effect of Pyrite on Resistivity and Other Logging Measurements, SPWLA 17th Annual Logging Symposium, Society of Petrophysicists and Well-Log Analysts

Clennell, M. B., Josh, M., Esteban, L., Piane, C. D., Schmid, S., Verrall, M., Hill, D., Woods, C., & McMullan, B., 2010, The Influence of Pyrite on Rock Electrical Properties: A Case Study from NW Australian Gas Reservoirs, SPWLA 51st Annual Logging Symposium, Society of Petrophysicists and Well-Log Analysts

Comisky, J. T., Santiago, M., McCollom, B., Buddhala, A., & Newsham, K. E., 2011, Sample Size Effects on the Application of Mercury Injection Capillary Pressure for Determining the Storage Capacity of Tight Gas and Oil Shales, Society of Petroleum Engineers. doi:10.2118/149432-MS

Donadille, J. M., Leech, R., & Pirie, I., 2016, Water Salinity Determination Over an Extended Salinity Range Using a Joint Interpretation of Dielectric and Neutron Cross-Section Measurements, SPE Annual Technical Conference and Exhibition, Society of Petroleum Engineers. doi:10.2118/181366-MS

Ferraris, P., Borovskaya, I., & Ribeiro, M., 2012, Advances in Formation Evaluation Independent of Conveyance Method: State of the Art Logging While Drilling & Wireline Petrophysical Analysis in a Carbonate Reservoir Offshore Brazil, SPWLA 53rd Annual Logging Symposium, Society of Petrophysicists and Well-Log Analysts

Gilmore, R.J., Clark, B., & Best, D., 1987, Enhanced Saturation Determination Using the EPT-G Endfire Antenna Array, SPWLA 28th Annual Logging Symposium, Society of Petrophysicists and Well-Log Analysts

Glover, P.W.J., Gomez, J.B., & Meredith, P.G., 2000, Fractures in saturated rocks undergoing triaxial deformation using complex electrical measurements, Earth and Planetary Science Letters, 183, 201–213

Han, Y., & Misra, S., 2017, Improved water-saturation estimates derived from inversion-based interpretation of broadband electromagnetic dispersion logs in organic-rich shale formations,

87th Annual International Meeting, SEG, Expanded Abstracts, 3458-3462, Society of Exploration Geophysicists

Han, Y., & Misra, S., 2018a, A unified inversion scheme to process multifrequency measurements of various dispersive electromagnetic properties, Journal of Applied Geophysics, 151, 23-39

Han, Y., & Misra, S., 2018b, Bakken Petroleum System Characterization Using Dielectric-Dispersion Logs, Society of Petrophysicists and Well-Log Analysts, 59(02), 201-217

Han, Y., & Misra, S., 2018c, Joint petrophysical inversion of multifrequency conductivity and permittivity logs derived from subsurface galvanic, induction, propagation, and dielectric dispersion measurements, Geophysics, 83(3), D97-D112

Han, Y., Misra, S., & Simpson, G., 2017, Dielectric Dispersion Log Interpretation in Bakken Petroleum System, SPWLA 58th Annual Logging Symposium, Society of Petrophysicists and Well-Log Analysts.

Knight, R. J., & Nur, A., 1987, The dielectric constant of sandstones, 50 kHz to 4 MHz: Geophysics, 52, 644-654

Misra, S., & Han, Y., 2016, Petrophysical Interpretation of Multi-Frequency Electromagnetic Measurements in Clay- and Conductive-Mineral-Rich Mudrocks, Unconventional Resources Technology Conference. doi:10.15530/URTEC-2016-2433541

Misra, S., Torres-Verdín, C., Homan, D., Minerbo, G., & Rasmus, J., 2015, Laboratory investigation of petrophysical applications of multi-frequency inductive-complex conductivity tensor measurements, SPWLA 56th Annual Logging Symposium, Society of Petrophysicists and Well-Log Analysts

Misra, S., Torres-Verdín, C., Revil, A., Rasmus, J., & Homan, D., 2016a, Interfacial polarization of disseminated conductive minerals in absence of redox-active species—Part 1: Mechanistic model and validation, Geophysics, 81(2), E139-E157

Misra, S., Torres-Verdín, C., Revil, A., Rasmus, J., & Homan, D., 2016b, Interfacial polarization of disseminated conductive minerals in absence of redox-active species—Part 2: Effective electrical conductivity and dielectric permittivity. Geophysics, 81(2), E159-E176

Misra, S., Luling, M., Rasmus, J., Homan, D., & Barber, T., 2016c, Dielectric effects in pyrite-rich clays on multi-frequency induction logs and equivalent laboratory core measurements, SPWLA 57th Annual Logging Symposium, Society of Petrophysicists and Well-Log Analysts

Newsham, K., Hanna, R., Lee, R., Whitney, C., & Chemali, R., 2018, September 17, As-Received Core Electrical Properties Tests for Determining Formation Factor FF and Resistivity Index RI, Society of Petroleum Engineers. doi:10.2118/191476-MS

Norbisrath, J.H., 2016, Complex Resistivity Spectra in Relation to Multiscale Pore Geometry in Carbonates and Mixed-Siliciclastic Rocks, University of Miami, Open Access Dissertations

Peeters, M., & Holmes, A., 2014, Review of Existing Shaly-Sand Models and Introduction of a New Method Based on Dry-Clay Parameters, Society of Petrophysicists and Well-Log Analysts, 55(6), 543–553

Pirie, I., Horkowitz, J., Simpson, G., & Hohman, J., 2016, Advanced methods for the evaluation of a hybrid-type unconventional play: The Bakken petroleum system. Interpretation, 4 (2): SF93–SF111

Sabouroux, P., & Ba, D., 2011, Epsimu, a Tool for Dielectric Properties Measurement of Porous Media: Application in Wet Granular Materials Characterization, Progress in Electromagnetic Research B, 29, 191-207

Salem, H.S., 2001, Determination of porosity, formation resistivity factor, Archie cementation factor and pore geometry factor for a glacial aquifer. Energy Sources, 23, 589–596

Sanchez-Ramirez, J.A., Torres-Verdín, C., Wang, G.L., Mendoza, A., Wolf, D., Liu, Z., & Schell, G., 2010, Field examples of the combined petrophysical inversion of gamma-ray, density, and resistivity logs acquired in thinly-bedded clastic rock formations, Society of Petrophysicists and Well-Log Analysts, 51, 247–263

Sarihi, A., & Murillo, B., 2015, A Method to Compute Water Saturation in Tight Rocks Accounting for Conductivity of Clay Minerals, SPE Annual Technical Conference and Exhibition, Society of Petroleum Engineers

Seleznev, N.V., Fellah, K., Philips, J., Zulkipli, S.N., & Fournie, B., 2014, Matrix Permittivity Measurements for Rock Powder, SPE Annual Technical Conference and Exhibition, Society of Petroleum Engineers.

Sherman, M.M., 1988, A model for the frequency dependence of the dielectric permittivity of reservoir rocks, Society of Petrophysicists and Well-Log Analysts, 29, 358–69

Somayeh K., 2017, Pore-scale assessment of Middle Bakken reservoir using centrifuge, mercury injection, nitrogen adsorption, NMR, and resistivity instruments, Colorado School of Mines, PhD Dissertation

Stroud, D., Milton, G.W., & De, B.R., 1986, Analytical model for the dielectric response of brine-saturated rocks, Physical Review B, 34, 5145- 5153

Tathed, P., Han, Y., & Misra, S., 2018a, Hydrocarbon saturation in upper Wolfcamp shale formation, Fuel, 219, 375-388

Tathed, P., Han, Y., & Misra, S., 2018b, Hydrocarbon saturation in Bakken Petroleum System based on joint inversion of resistivity and dielectric dispersion logs, Fuel, 233, 45-55

Tiab, D., & Donaldson, E. C., 2004, Petrophysics: Theory and practice of measuring reservoir rock and fluid transport properties, Gulf Professional Pub

Waxman, M.H., & Smits, L.J., 1968, Electrical Conductivities in Oil-Bearing Shaly Sands, Society of Petroleum Engineers, 8(2), 107-122

Zhang, B., & Xu, J., 2016, Methods for the evaluation of water saturation considering TOC in shale reservoirs, Journal of Natural Gas Science and Engineering, 36, 800–10

Appendix A: Dielectric EM Laboratory Measurements on Sandstone Samples

A.1 Abstract

This chapter provides literature review on the dielectric measurements performed on conventional rocks and the fundamentals of dielectric permittivity. We present porosity, saturation, Nuclear Magnetic Resonance (NMR) measurements carried out on Berea sandstone samples. We further performed dielectric measurements on dry, deionized (DI) water saturated and brine saturated samples to characterize dielectric polarization phenomena.

A.2 History of EM measurements on Sandstone

Complex dielectric permittivity (ε^*) measurements in the frequency range of 0.001 Hz to 10 GHz are widely used for the oil and gas, hydrological, and various other geological applications (Gilmore et al., 1987, Sherman, 1988). ε^* is a fundamental material parameter that affects the propagation of electric fields. It is a measure of electrical charge storage (polarization) in a material in response to an external electric field. Dielectric permittivity of any material typically exhibits frequency dependence and is a complex-valued parameter because a material's response in form of an induced polarization lags the applied field. For measurements at low frequencies, the phase and imaginary component of ε^* is close to zero. As the frequency increases, a measurable phase and imaginary component emerges in ε^*. The real part of ε^*, represented as ε', is related to the stored electromagnetic energy within the material in the presence of applied field, whereas the imaginary part of ε^*, represented as ε'', is related to dissipation of the applied electromagnetic energy within the material, such that

$$\varepsilon^*(\omega) = \varepsilon'(\omega) + \mathrm{i}\varepsilon''(\omega), \qquad (A.1)$$

where ω is the angular frequency of the applied electric field.

Frequency dependence of ε^* leads to frequency dispersion in ε', ε'', permittivity magnitude ($|\varepsilon|$), and permittivity phase angle (θ). For fluid-filled porous geomaterials, frequency dispersion is due to the occurrence of various polarization phenomena, such as orientation or dipolar polarization of dipoles in fluids, Maxwell-Wagner (MW) polarization at brine-matrix interface, interfacial polarization of conductive minerals (Misra et al., 2016b), membrane or double-layer polarization of clays and surface-charge-bearing grains (Misra et al., 2016a), and concentration polarization due to differential mobilities of ions present in fluid. Each polarization mechanism is dominant within a distinct frequency range. For example, MW polarization and orientation polarization influences frequency dispersion in 1 kHz to 30 MHz in fluid-filled porous geomaterials in the absence of conductive minerals, surface-charge-bearing-grains, and clays (Misra et al., 2016c).

A.3 Samples Description

We extracted 10 cylindrical samples of 1.625 inches in diameter and 5.5mm to 9mm in thickness, and 4 cylindrical samples of 1 inch in diameter and 6.4 mm to 10 mm in thickness from a Berea sandstone block. Table A.1 gives the exact dimensions of these 14 samples. All the extracted samples were further polished using a surface grinding machine with surface grit 220-320 to reduce the effects of surface roughness on permittivity measurements. Three of the first set of 10 samples were cleaned for 24 hours using Soxhlet apparatus to remove hydrocarbon and salt present in the connected pore spaces of the sample. A mixture of toluene and methanol (80:20) was used as the extraction solvent in the Soxhlet apparatus. The three samples were kept in an oven at 100˚C for 24 hours to complete the cleaning process.

Table A.1 Dimensions of 14 Berea Sandstone samples

Sample/Cleaning	Diameter (mm)	Thickness (mm)	Mass before saturation (gm)	Mass after saturation (gm)
S1-Uncleaned	41.325±0.02	9.1±0.01	24.4	26.93
S2-Uncleaned	41.235±0.005	8.2±0.0005	21.96	24.21
S3-Uncleaned	41.71±0.02	6.8±0.02	18.42	20.35
S4-Uncleaned	41.71±0.06	6.42±0.01	17.37	19.23
S5-Uncleaned	41.69±0.02	7.54±0.01	20.35	22.49
S6-Uncleaned	41.67±0.03	7.75±0.02	20.96	23.18
S7-Uncleaned	41.63±0.03	9.09±0.008	24.7	27.3
S8-Cleaned	41.17±0.008	7.28±0.02	19.34	21.15
S9-Cleaned	41.235±0.05	5.59±0.05	14.73	16.56
S10-Cleaned	41.13±0.022	5.795±0.06	15.34	17.2
S11-Uncleaned	25.12±0.06	6.57±0.007	6.41	8.34
S12-Uncleaned	25.12±0.03	7.41±0.007	7.31	9.34
S13-Uncleaned	25.12±0.08	7.72±0.02	7.51	9.65
S14-Uncleaned	25.12±0.09	7.625±0.03	7.41	9.56

A.4 Measurements on saturated samples

Porosity

Dry porosity measurements were carried out on 1-inch-diameter sample using Coretest Systems's AP608 Porosimeter (Automated Permeameter) and High-Pressure Pycnometer (HPP). AP608 porosimeter measures the confined porosity and pore volume using Boyle's law technique. A standard stainless steel non-porous plug with known dimensions and bulk volume, is used to calibrate AP608 porosimeter. Confined dry porosities of a sample were measured at a pore pressure of 200 psi and various confined pressures in the range of 500 psi to 2500 psi. HPP measures unconfined grain volume using Boyle's Law technique. A porous calcite sample of known grain density was used to calibrate the HPP apparatus. First, the grain volume of a sample at ambient conditions was measured using HPP. Following that, bulk volume of the sample at ambient conditions was obtained based on Archimedes' principle using liquid mercury. Porosity of the

sample at ambient conditions was then calculated from the grain volume and bulk volume measurements.

Saturation and NMR

We used standard saturation core holder, syringe pump (Teledyne ISCO), vacuum pump, and pump controller (Model 65D) for saturating Berea sandstone samples. We fully saturated the 14 samples with DI-water of conductivity 0.11 mS/m at 22˚C. After saturation, samples are stored in a container filled with DI-water at ambient conditions. After performing the dielectric measurements, the DI-water-saturated samples were oven dried for 24hours at 100˚C. Following that, the samples were further saturated with 0.5% KCl brine of conductivity 0.8 S/m at 24˚C. Table A.1 mentions the mass of the samples measured before and after saturating with brine.

Water-filled porosity and water-filled pore-size distribution were measured using 12 MHz Oxford Geospec NMR spectrometers. NMR measurements were calibrated based on the known pore volume response of 2% NaCl. Samples saturated with brine were precisely placed in the portion of homogeneous magnetic field. The initial parameters assumed for Berea sandstone samples include: (a) Signal-to-Noise Ratio of 50, (b) τ (time between 90 and 180 pulses in a CPMG sequence) of 57 μs, and (c) T2 relaxation time of 300 ms.

Dielectric Equipment Calibration

We use the Keysight 16451B dielectric fixture because the guard electrodes can minimize stray capacitance that develops at the edge of electrodes. We performed adapter setup, cable length compensation, open correction, short correction and load compensation to reduce residual impedance and stray admittance on dielectric test fixture 16451B and impedance analyzer E4990A (Figure A.1). E4990A measurements exhibit 10% or less accuracy for sample impedance in the

range of 50 mΩ to 40 MΩ in the frequency range of 20 Hz to 100 MHz. We also carried out several adjustments to make the electrodes parallel to each other. For materials having low dielectric constant, it is recommended that the larger-diameter electrode A of diameter 38 mm be used instead of the electrode B of diameter 5 mm.

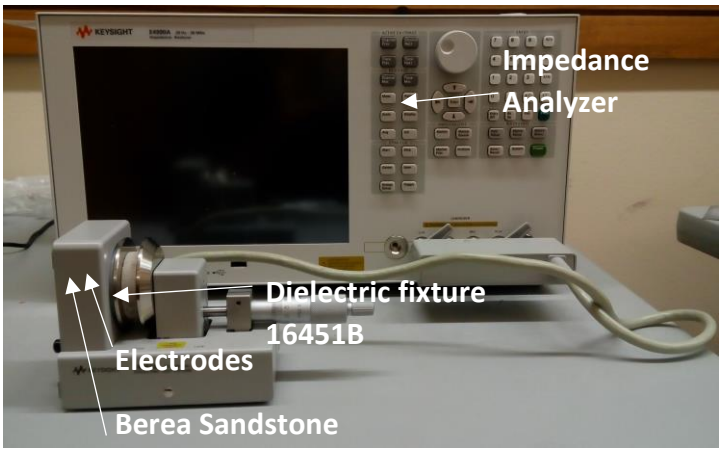

Figure A.1 Dielectric Fixture 16451B and Impedance Analyzer E4990A setup

Dielectric Measurement

Complex dielectric permittivity of S1-S10 samples were measured using the Contact Electrode Method and the Non-Contact Electrode method in the frequency range of 1 kHz to 30 MHz. Measurements below 1 kHz are considered less reliable since the accuracy of the impedance analyzer E4990A crosses the threshold for acceptable accuracy of 0.1% for sample impedance in the range of 10 Ω to 100 kΩ. Non-Contact method in comparison to the Contact method typically reduces error in presence of air gaps due to surface roughness and irregularities on the surface in contact with the electrodes.

In theory, the dielectric tool setup first measures the complex impedance (Z^*) of the material sample, which is expressed as

$$Z^* = R_s + jX_s, \qquad (A.2)$$

where R_s is the resistance and X_s is the reactance of the material (Knight and Nur, 1987). Complex admittance (Y^*) of the material sample is expressed as

$$Y^* = (Z^*)^{-1}, \quad (A.3)$$

which is used to compute the complex dielectric permittivity of porous geomaterials, such that

$$\varepsilon_r{}^* = \frac{Y^*}{i\varepsilon_0\omega}\frac{t}{A}, \quad (A.4)$$

where t is thickness of the sample, A is the cross-sectional area of the sample, ω is the angular frequency, and ε_0 is the vacuum permittivity equal to 8.85 x 10^{-12} F/m.

A.5 Results

The confined porosity of a dry Berea sandstone sample measured using AP608 Porosimeter, as shown in Figure A.2, is negatively correlated with the confining pressure from 500-2700 psi. In another method of porosity estimation on the same sample, the grain volume of the dry sample measured using HPP was 3.7 cc and the bulk volume measured by immersion in a mercury bath was 4.8 cc. Thus, the sample porosity obtained using this method was 22.9%. The sample was saturated with KCl solution of conductivity 1.19 $\mu S/cm$ (0.59 ppm), and the NMR-measured cumulative brine-filled porosity of the sample was 22%, as shown in Figure A.2b. NMR water-filled porosity for rest of the samples followed same trend. The porosity obtained from HPP agreed with AP-608 porosity and NMR water-filled porosity within ±1 porosity unit for all the samples.

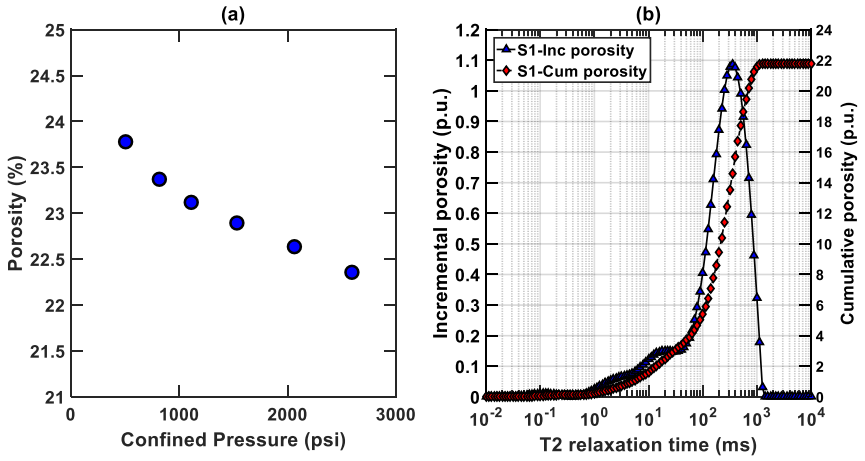

Figure A.2 (a) Porosity at various confining pressures and (b) NMR measured values of incremental and cumulative porosities for sample S1

The magnitude of relative permittivities of dry, DI-water-saturated and brine-saturated Berea sandstone samples decrease with increase in frequency. For dry samples, as shown in Figure A.3, relative permittivity decreases from 18 to 3.7 and phase from 37˚ to 2.2˚ in the frequency range of 1 kHz to 30 MHz. With the increase in fluid salinity, permittivity and phase increases. For DI-water-saturated samples, relative permittivity decreases from 9500 to 10.5 in the measured frequency range. With an increase in conductivity of the saturating fluid, relative permittivity increases by 10 times at lower frequencies and by 5 times at higher frequencies. For the brine-saturated samples, relative permittivity varies from 10^5 to 29 in the measured frequency range. Variations in relative permittivity are larger at low frequencies compared to those at high frequencies for DI-water-saturated and brine-saturated Berea sandstone samples, whereas dry samples show negligible variations in relative permittivity in the measured frequency range. In absence of electrode polarization effects, the large frequency dispersion and large permittivity values measured for the fluid-saturated samples can be explained using the MW polarization mechanism. With increase in frequency, the magnitude of relative permittivity decreases, and the phase angle shows peak, which are characteristics of various relaxation processes. On the other

hand, at low frequencies, variations in phase are larger for dry samples in comparison to those for DI-water-saturated and brine-saturated samples. For fluid-saturated samples, for a decrease in frequency from 10^5 Hz to 10^4 Hz and 10^6 Hz to 10^5 Hz, respectively, the phase angle increases owing to conduction phenomena.

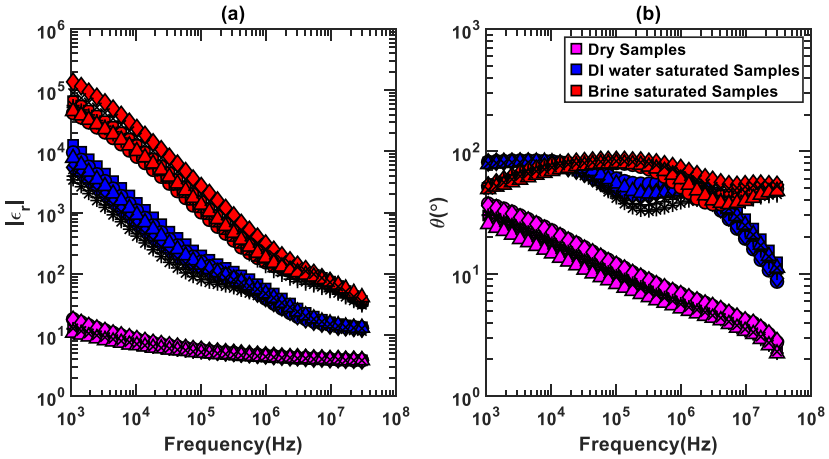

Figure A.3 (a) Magnitude and (b) phase of relative permittivity of dry, DI-water-saturated and brine-water saturated samples: S1(circle), S2diamond), S3(plus), S4(asterisk), S5(triangle), S6(cross), and S7(square).

A.6 Conclusion

We measured the dielectric response of 14 Berea sandstone samples over a frequency range of 1 kHz to 30 MHz at ambient temperature and pressure conditions. These samples were studied in three states:dry, saturated with DI water, and saturated with brine. The dielectric constant of dry, DI-water-filled, and brine-filled samples vary smoothly from 3.5 to 15, 3.5 to 2000, and 20 to 10^5, respectively, for a continuous reduction in frequency of measurement from 30 MHz to 1 kHz. The large frequency dispersion of relative dielectric permittivity and phase angle can be explained based on the MW polarization mechanism for frequencies higher than 1 kHz. Salinity due to brine influences MW polarization as more charges can accumulate at the interface. Therefore, Berea

sandstone samples saturated with brine produces higher permittivity dispersion than samples saturated with DI-water.

Appendix B. Laboratory Resistivity Measurements on Wolfcamp Shale Samples

B.1 Abstract

This chapter focusses mainly on the electrical resistivity measurement performed on Wolfcamp samples. We analyze the effect of different confining pressure and equilibrium time on the complex electrical resistivity of the saturated samples. We further use the conventional equations to calculate the formation factor and cementation exponent for these samples.

B.2 History of resistivity measurements on shale

Hydrocarbon saturation is an important parameter during reservoir development. Electrical logging is widely used to determine hydrocarbon saturation. Archie (1942) established algorithm in clay-free reservoirs, relating bulk resistivity (R_t) to porosity (φ), formation water resistivity(R_w) and water saturation(S_w) as,

$$R_t = \frac{aR_w}{\varphi^m S_w^n} \tag{B.1}$$

where a is the tortuosity factor, m is the cementation exponent, and n is the saturation exponent. Cementation exponent m relates to the pore tortuosity, and saturation exponent n reflects the wettability of matrix and distribution of fluids within pores (Tiab, 2004). Formation factor (FF) is denoted as the ratio of formation resistivity at 100% brine saturated (R_o) with connate water resistivity (R_w),

$$FF = \frac{R_o}{R_w} = \frac{1}{\varphi^m} \tag{B.2}$$

To estimate water saturation, R_t and φ are computed from or measured from well logs, whereas m, n, and R_w are estimated from core laboratory experiments and inter-well correlation. Newsham

et al. (2018) conducted a resistivity measurement workflow to determine formation factor and resistivity index in Wolfcamp and Avalon samples. Cementation exponent value was 2.08 and log based computed water saturation matched with the estimated core water saturation. Somayeh (2017) determined geometrical tortuosity of pore network and cementation exponent from the resistivity measurements for Middle Bakken cores to lie in the range of 12-18 and 1.92-2.17, respectively. Geometrical tortuosity is expressed as the ratio of length of flow path between two points to the straight-line distance between those two points.

There is a need for new systematic experimental study of resistivity measurements at low frequency on shale samples with ultra-low permeability, low porosity and high clay content. Further sections highlight the electrical resistivity measurements on Wolfcamp samples.

B.3 Samples Description

We received 5 cylindrical samples of 1.00 inch in diameter and 0.84 to 1.44 in thickness from Upper Wolfcamp in Delaware basin. Table B.1 gives the exact dimensions of these 5 samples. Measured total organic carbon (TOC) content on these 5 samples is within a range of 1.26-8.9 wt%. A low-pressure pycnometer (LPP) is used to measure absolute porosity with porosities reproducible to better than ±0.5 p.u. (Comisky et al., 2011). The AccuPyc 1330 pycnometer uses gas displacement method that determines the density and volume of the sample. Porosity ranges from 5.8-10.2 p.u., with sample 242H having the highest porosity of 10.2 p.u.

Fourier transform infrared spectroscopy (FTIR) was also performed on a portion of each sample ensuring the section was representative. All samples were analyzed with a consistent methodology and multiple runs to ensure data quality. The runs were then quality checked and processed to produce sixteen normalized mineral fractions which include quartz, orthoclase feldspar, oglioclase

feldspar, calcite, dolomite, pyrite, illite, mixed clays, chlorite, kaolinite, smectite, albite, anhydrite, siderite, apatite, and aragonite as represented in Figure B.1.

Table B.1 Dimensions of 5 Wolfcamp samples

Sample	Diameter (inch)	Thickness (inch)	Mass before saturation (gm)	Mass after saturation (gm)	TOC (wt%)	LPP (p.u.)
242H	1	0.84±0.001	25.78	26.78	1.26	10.23
245H	1	1.4±0.001	45.28	46.44	5.21	8.07
252H	1	0.99±0.002	31.42	31.97	5.22	7.84
256H	1	0.89±0.001	29.3	29.78	8.92	5.88
259H	1	0.88±0.001	24.92	25.64	3.19	9.82

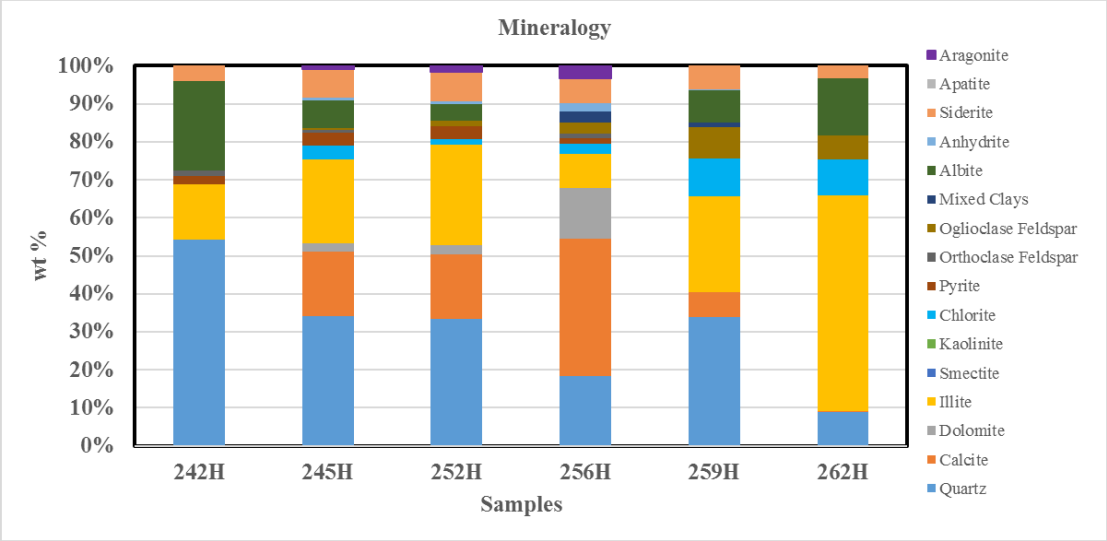

Figure B.1 FTIR Mineralogy of Wolfcamp samples

B.4 Measurements on saturated samples

Saturation and NMR

We used standard saturation core holder, syringe pump (Teledyne ISCO), vacuum pump, and pump controller (Model 65D) for saturating Wolfcamp samples. We fully saturated the 5 samples with deionized (DI) water of conductivity 2S/m at 7000psi for 48 hours. After saturation, samples

are stored in a container filled with DI-water at ambient conditions. Table B.1 mentions the mass of the samples measured before and after saturating with brine.

Water-filled porosity and water-filled pore-size distribution of the samples were measured using 12 MHz Oxford Geospec Nuclear Magnetic Resonance (NMR) spectrometers. NMR measurements were calibrated based on the known pore volume response of 2% NaCl. Samples saturated with brine were precisely placed in the portion of homogeneous magnetic field. The initial parameters assumed for Wolfcamp samples include: (a) Signal-to-Noise Ratio of 50, (b) τ (time between 90 and 180 pulses in a CPMG sequence) of 57 µs, and (c) T2 relaxation time of 300 ms.

Resistivity Measurement

Resistivity of Wolfcamp samples were measured using NER Autolab resistivity cell in the frequency range of 20 Hz to 200 kHz. Filler papers are placed across the sample to prevent contact with oil, which provides uniform confining pressure around the sample. The resistivity measurements were performed at confining pressure of 3500-4500 psi. Extreme caution must be taken while handling the sensitive sample holder, as the electrodes are sensitive. Electrode polarization and electromagnetic coupling can cause significant error in this two-electrode measurement.

B.5 Experiment Results

Effect of confining pressure and equilibrium time

Figure B.2 represents magnitude of resistivity for 100% saturated samples. Resistivity dispersion was observed, with resistivity decreasing with increase in frequency. All rocks showed increase in resistivity with increase in confining pressure and increase in equilibrium time. This has been noted by researchers in sandstone samples. (Glover et al., 2000) suggested that clay-rich sandstones

showed greater pressure sensitivity than clean rich sandstones due to the closure of low aspect ratio pores located at grain contacts and associated with clay minerals. Figure B.3 represents relative resistivity change for sample 242H, which has 14% clay content and sample 252H that has 27% clay content. Resistivity change has been calculated as the ratio of resistivity in the initial state to resistivity in the final state. Final state for sample 242H is noted at 3500psi confining pressure after 2 hours and for sample 252H at 4500psi confining pressure after 2 hours. Sample 242H has decrease in relative resistivity change with increase in frequency, while for 252H there is an initial increase in relative resistivity change with increase in frequency till 10kHz.

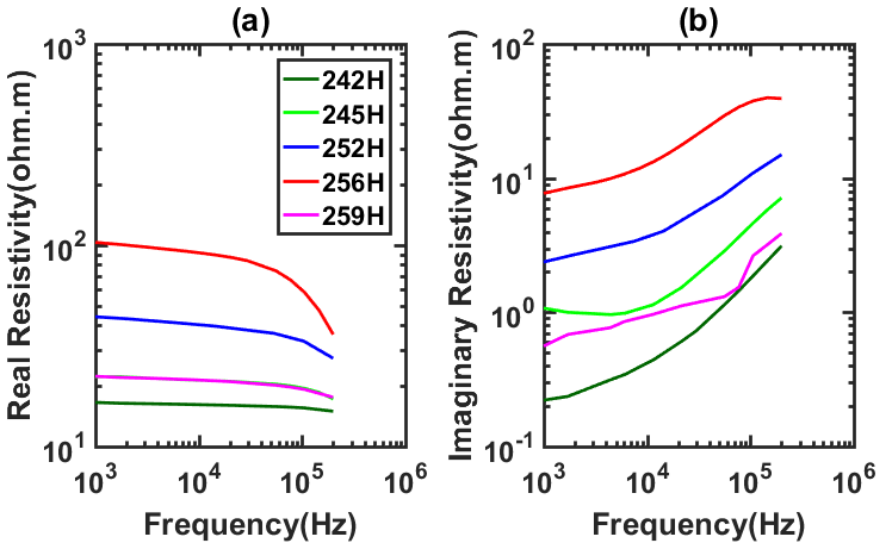

Figure B.2 (a) Real part of resistivity (b) Imaginary part of resistivity for samples 242H, 245H, 252H, 256H and 259H

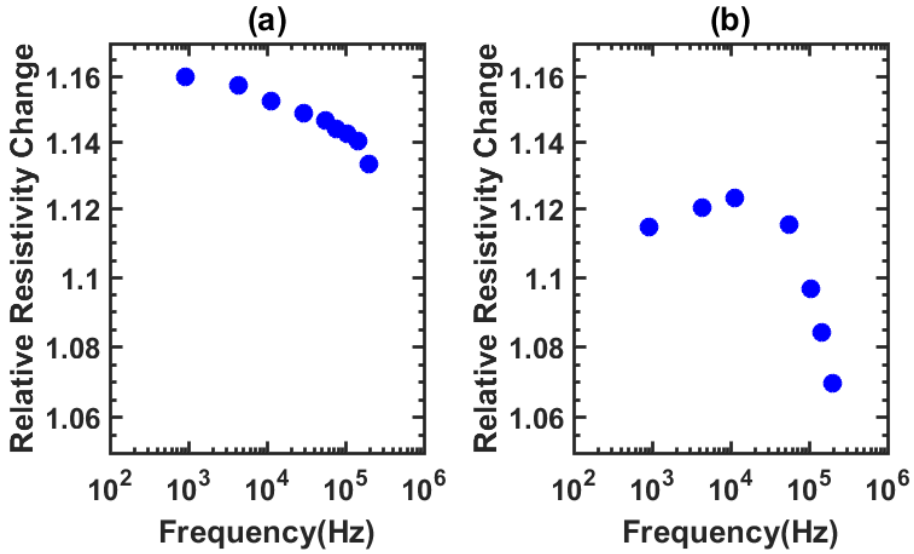

Figure B.3 Relative resistivity changes with frequency for (a) sample 242H at 3500psi confining pressure and (b) sample 252H at 4500psi confining pressure and 2 hours of equilibrium time.

Resistivity and porosity

Figure B.4 shows a cross-plot of resistivity and formation factor with porosity for Wolfcamp samples. Formation resistivity factor is a function of several physical parameters and lithological attributes (Salem, 2001). The ratio of formation resistivity factor F as represented in Equation 3.2 and log of porosity, $\log(\varphi)$, is the Archie porosity exponent, m. These porosity exponent values assume an Archie intercept, a = 1. It turns out to be a good correlation with R^2 =0.81 from linear least square regression. The cross-plot computes cementation exponent which reflects influence of pore geometry on resistivity.

Water saturation can be influenced by the existence of TOC, and hence it plays and important role in calculation of shale reservoir (Zhang and Xu, 2016). Figure B.5 shows a cross-plot of porosity and TOC with cementation exponent for Wolfcamp samples. Cementation exponent decreases as the porosity increases, whereas higher TOC samples show higher cementation factor. This tendency has been observed in carbonates as the tendency of kerogen developed nano-vugs when maturity increased (Norbisrath, 2016).

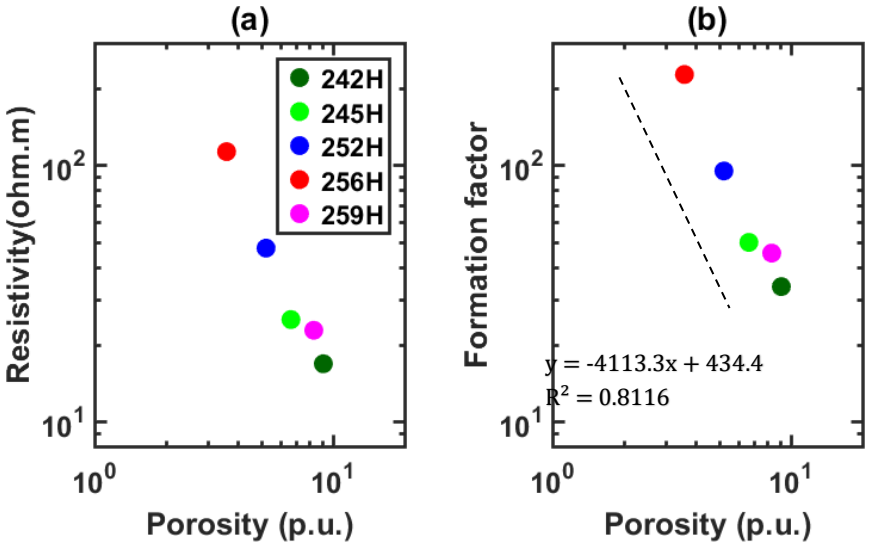

Figure B.4 Cross-plot of (a) resistivity and porosity for Wolfcamp samples at 1000Hz frequency (b) formation factor and porosity on log-log scale at 1000Hz frequency

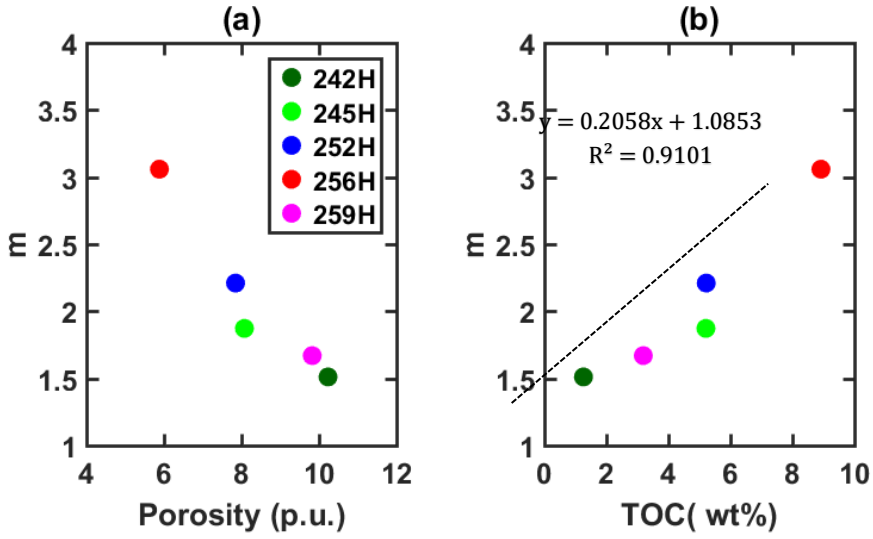

Figure B.5 Cross-plot of (a) cementation exponent and porosity for Wolfcamp samples (b) cementation exponent and total organic carbon

B.6 Conclusion

We measured electrical resistivity of Wolfcamp samples from 20 Hz to 200 kHz. Resistivity dispersion was observed in saturated samples, with magnitude of resistivity decreasing as

frequency increased. With increase in confining pressure and time, increase in resistivity was observed. Sample 242H showed decrease in relative resistivity change with increase in frequency, while 252H showed initial increase in relative resistivity change with increase in frequency till 10kHz. Our results provide empirical relationship between formation factor and porosity.